ACTIVE LUBRICATION INTERFACES WITH TUNABLE MICRO-TEXTURES

A THESIS SUBMITTED TO

THE GRADUATE SCHOOL OF ENGINEERING AND SCIENCE

OF BILKENT UNIVERSITY

IN PARTIAL FULFILLMENT OF THE REQUIREMENTS FOR

THE DEGREE OF

MASTER OF SCIENCE

IN

MECHANICAL ENGINEERING

By

Sena Pekol

July 2023

Active Lubrication Interfaces with Tunable Micro-Textures
By Sena Pekol
July 2023

We certify that we have read this thesis and that in our opinion it is fully adequate, in scope and in quality, as a thesis for the degree of Master of Science.

İlker Temizer (Advisor)

Luca Biancofiore

Ercan Gürses

Approved for the Graduate School of Engineering and Science:

Orhan Arıkan
Director of the Graduate School

ABSTRACT

ACTIVE LUBRICATION INTERFACES WITH TUNABLE MICRO-TEXTURES

Sena Pekol
M.S. in Mechanical Engineering
Advisor: İlker Temizer
July 2023

This thesis investigates a homogenization-based space-time optimization framework in the context of hydrodynamic lubrication in order to design micro-textures which can be actively controlled through external stimuli. The response at the interface is established via the Reynolds equation to describe the physics of the lubrication for a small film thickness. Subsequently, the interface is subjected to multiscale analysis and effective macroscopic parameters are derived via homogenization method. In order to calculate the macroscopic parameters, Finite Element (FE) formulation is employed and the implementation of the parameters in the in-house FE code is demonstrated. For the suboptimality problem due to typically employed fixed unit cell in FE analysis, a geometry optimization scheme is developed. Thereafter, a sensitivity based topology optimization framework is introduced with the aim of identifying the spatial distribution and temporal variation of the micro-texture, and the shape of the unit cell which together help achieve the targeted lubrication response. The performance of the employed framework is assessed through objectives which ultimately determine the macroscopic flux at the interface as well as the frictional traction that is associated with the macroscopic dissipation at the interface. Finally, three-dimensional realizations are constructed for active micro-textures by adopting a readily deployable experimental architecture.

Keywords: Topology optimization, homogenization, hydrodynamic lubrication, micro-texture design, tunability.

ÖZET

AYARLANABİLİR MİKRO-DESEN TABANLI AKTİF YAĞLAMA ARAYÜZEYLERİ

Sena Pekol
Makine Mühendisliği, Yüksek Lisans
Tez Danışmanı: İlker Temizer
Temmuz 2023

Bu tezde, hidrodinamik yağlama problemleri için dış uyaranlarca kontrol edilebilen aktif desen tasarımı için türdeşleştirme temelli konum-zaman mikroyüzey eniyilemesi araştırılmaktadır. Yağlama fiziğini nitelendirmek adına arayüz davranışı ince film varsayımı altında Reynolds denklemi kullanılarak elde edilmiştir. Takibinde, arayüz çok-ölçekli analize tabi tutulmuş ve makroskopik parametreler türdeşleştirme yöntemi ile türetilmiştir. Makroskopik parametrelerin hesaplanması için sonlu elemanlar (SE) formülasyonu kullanılmış ve parametrelerin çalışmaya ait kod implementasyonu gösterilmiştir. SE analizinde tipik olarak sabit tutularak kullanılan birim hücre yol açtığı yetersiz iyileştirme sorununu engellemek amacıyla, sisteme dahil bir geometri eniyilemesi geliştirilmiştir. Sonrasında, istenilen yağlama davranışını gösteren aktif mikroyüzeyler bulunması gayesi ile, mikroyüzeyin konumsal dağılımını, zamana bağlı değişimini ve birim eleman şeklini belirleyebilecek hassasiyet tabanlı bir topoloji eniyileme sistemi tanıtılmıştır. Kullanılan sistemin performansı, arayüzdeki makroskopik enerji yitimi ile ilişkilendirilmiş, makroskopik akı ve sürtünme vektörü tabanlı objektiflerin belirlenmesi ile ölçülmüştür. Son olarak, halihazırda uygulanabilecek deneysel bir mimari benimsenerek aktif mikro desenler üç boyutlu olarak kurulmuştur.

Anahtar sözcükler: Topoloji eniyilemesi, türdeşleştirme, hidrodinamik yağlama, mikro-desen tasarımı, ayarlanabilirlik.

Acknowledgement

I thank Prof. İlker Temizer for his never-ending patience and assistance with his evergreen enthusiasm for learning and teaching. I am grateful for his guidance on every step of the way and for the invaluable lessons I will cherish for the rest of my career.

I thank my dearest friend Senem, her endurance was and always be inspiring. I am forever thankful to Elif, Candan, Alper, Uzay and Önder for the bittersweet, yet precious memories. Also to Berkan, he is the one to call for an interesting scientific discussion, probably a long one.

My deepest gratitude to my family; to my sister Eda for always lifting my spirit, my mother Nermin for always being there for me and my father Mustafa for always supporting me in his own unique way.

I also thank for the financial support from TUBİTAK BİDEB 2210-C programme.

Contents

List of Figures

List of Tables

Chapter 1

Introduction

Tribology has been an engaging field to study, with applications on wear, friction and lubrication [2–5]. Design, analysis and manufacturing for these applications require careful investigations on parameters such as surface topography, interface geometry and material selection. In addition, with the recent popularity of smart materials which have temporal properties [1, 6–14], tribological studies widen their potential application fields and therefore made the investigation methods more and more important. Therefore in this work, the concept of stimuli-responsive active micro-texture design is introduced in the context of hydrodynamic lubrication. The introduced methodology primarily focuses on the utilization of topology optimization along with a Reynold equation based homogenization framework to design active textures. Subsequently, the viability of the idea is demonstrated by executing three-dimensional (3D) realizations of the active textures based on available experimental frameworks [1, 8]. Overall, an efficient and comprehensive design methodology is proposed for hydrodynamically lubricated active textures.

Since the early studies, lubrication is used for reliable design and manufacturing in different areas [2–4]. Starting from the attempts on enhancing machinery performance, hydrodynamic lubrication has gained a wide range of usage including magnetic storage devices, MEMS/NEMS and biomedical applications [3, 5].

In order to design such interfaces, there have been studies that work on the texture shape for the optimal lubrication conditions. Some studies worked on improving the load carrying capacity of the interface [15, 16]. Friction characteristics have also been studied for textured surfaces based on various texture shapes, interface geometry and lubricant parameters [17–22]. As these studies demonstrate, the design and production of hydrodynamically lubricated surfaces carries a significant importance in the efficiency of the existing systems and on novel applications.

The optimization of hydrodynamically lubricated surfaces was first studied by Lord Rayleigh where he discussed the effect of geometric parameters on the applied force and maximum load capacity for a given minimum film thickness [23]. Since then, there have been various studies on the optimization of interface parameters for optimal lubrication conditions [24–39]. Among these, few studies invoke a non-parametric approach for the topology optimization in which whole structure is subjected to adjustments. This method is indicated to be more effective compared to parametric approaches [37]. Among the studies which use non-parametric approaches, there are sensitivity-based optimizations which are implemented as solid isotropic material penalization (SIMP) [30, 31, 35] or based on level-set [37]. Recently, a metaheuristic approach which uses machine learning to develop a universal design framework [40] has been introduced. Both sensitivity based and metaheuristic approaches have advantages and disadvantages. Sensitivity-based optimization frameworks are highly dependent on the initial configuration whereas metaheuristic optimization requires large amount of data to produce results. However, they are both shown to be effective for the texture design in lubrication problems. In this study, commonly used Method of Moving Asymptotes(MMA) is adapted which is a sensitivity-based nonlinear-optimization algorithm by Svanberg [41] and surface textures are obtained via topology optimization for the ideal lubrication response.

In order to invoke the optimization framework, the effect of the interface parameters to the lubrication response needs to be addressed. This effort was first initiated by experimental studies of Beauchamp Tower. Subsequently, Osborne Reynolds introduced Reynolds equation as a mathematical model for thin film flow. Since then, the Reynolds equation is widely used for the studies of lubrication [3]. On the other hand, considering the intrinsically multiscale structure of the interfaces where there is a macroscopically changing surface thickness and a micro-scale roughness, homogenization offers a versatile method to describe geometry dependent lubrication parameters. Recently, advantages of homogenization have also been discussed in comparison with the other extensively used method named averaged flow method by Cheng and Patir [42] for hydrodynamic lubrication, and homogenization is reported to be more effective [43]. Previous to this work, comparison of these two methods was performed where the rigorousness of homogenization method in hydrodynamic lubrication analysis was reported as well [44]. Homogenization with asymptotic expansion has been used in various fields to deliver effective properties on macroscale from the microscale [45–47]. For lubrication, two-scale analysis was introduced for the first time to capture microscopic and macroscopic alterations in the film thickness by Elrod [48]. The approach developed therein was able to capture earlier studies as special cases. Homogenization of Stokes system was introduced for rapidly varying film thickness for a viscous fluid by Bayada and Chambat in [49]. This approach was shown to be effective in describing the physics of hydrodynamic lubrication with Reynolds roughness and is used in several studies [30, 31, 35, 50, 51]. In view of these advantages, the homogenization of the Reynolds equation will also form the basis for obtaining effective parameters that will be employed in optimization.

It is noted that topology optimization framework along with the homogenization can encounter suboptimality problems due to restricted design space. For the hydrodynamic lubrication setting, angle of the grooves is demonstrated to influence the objective function and for intermediate angles, the produced designs might be suboptimal [35]. This issue has been previously addressed by Barbarosie and Toader [52] and it is shown that by adjusting the shape of the unit cell, the suboptimal results can be eliminated or reduced in the calculations. Recently, this approach is applied in a fully three-dimensional setting in the context of time-varying microscopic response [53]. Following a similar approach, a geometry optimization scheme is introduced to the numerical setup of this work.

Despite the significant advances towards interface micro-texture design, most studies focus on static interface geometries. Considering recent remarkable developments in the active materials, it is valuable to enhance the flexibility of the designs. Some of the numerous applications in which smart design methods can be implemented are mentioned here for the active surfaces. One of the significant developments in the field is 4D printing. It allows materials, which are external-stimuli sensitive, to be placed in 3D printed parts [6, 7]. Another way is to combine thin sheets of electrodes with an elastomer and allow a coupled deformation with an electric field [1, 8]. There are also light sensitive materials which are utilized for programmable topological responses [9]. Along with these advancements in tunable textures, various studies investigated controlled response of fluids via active change of the surface and the fluid properties. For instance, tunable surfaces were design to control wettability where by changing the surface texture, hydrophilicity of the surfaces could be altered [10, 11]. Rheological textures are investigated for magnetheorological fluids to control the yield stress and viscosity [12] and for the aim of active friction control, morphing surfaces are introduced [14]. Acknowledging the potential usage of active surfaces in various characteristics, topology optimization with homogenization offers a valuable design methodology. This work presents this strategy for active surfaces to catch the targeted lubrication response with a proof of concept application.

The thesis consists of following chapters: in Chapter 2, lubrication regimes are introduced and Reynolds equation is derived from Navier-Stokes equation. In Chapter 3, homogenization of Reynolds equation is given and homogenized coefficients are obtained along with the sensitivities with respect to texture change and the shape of the unit cell. In Chapter 4, finite element formulations are given for the cell problems and for the homogenized coefficients. In Chapter 5, optimization scheme is introduced where design variables, objective function and constraints are given. In Chapter 6, numerical results are presented where different optimization schemes and their contributions are explained in detail. In Chapter 7, results obtained from topology optimization are used to create three-dimensional examples and the final results are compared with the target responses. Concluding remarks and an outlook are provided in Chapter 8.

Chapter 2

Lubrication Theory

In this chapter, the Reynolds Equation is derived for an interface with small film thickness and the forms for the flux and traction are obtained.

2.1 Tribology and Lubrication

Tribology is the study which focuses on the lubrication, friction and wear of interacting surfaces which can be stationary or have a relative motion. In the context of tribology, fluids and solids can be employed as lubricants depending on the particular application. It is essential to describe the interaction between the lubricant and the surfaces of the interface in such applications.

For fluid film lubrication, there are several lubrication regimes which are hydrodynamic, elastohydrodynamic, boundary and mixed. Hydrodynamic lubrication (HL) typically happens when there are conformal surfaces. A pressure is developed, which is usually less than 5 MPa and does not cause a significant deformation. Typically, distance between the surfaces exceeds 1 μm so that the surface contact is prevented. This is also known as the ideal form of lubrication. Elastohydrodynamic lubrication (EHL) is a type of HL with eminent elastic deformation. It is associated with non-conformal surfaces and can be grouped as hard EHL where the surfaces have high elastic modulus such as metals and soft EHL where surfaces are more deformable such as rubber. In boundary lubrication (BL), surfaces are very close to each other, so that the lubricant thickness is insignificant and the response is dominated by the solid contact. Mixed (or, partial) lubrication is the transition between HL/EHL and BL where there are regions of contact but at least a portion of the interface is covered with a fluid lubricant. In this work, contact is neglected and hydrodynamic lubrication is studied in the absence of surface deformation.

2.2 Reynolds Equation

Reynolds equation describes the effective response for fluid film lubrication where the thickness of the fluid film is much smaller than the width of lubrication domain. In this section, the derivation of the Reynolds equation is briefly outlined starting from Navier-Stokes equation

$$\rho(\frac{\partial \boldsymbol{v}}{\partial t} + (\nabla \boldsymbol{v})\boldsymbol{v}) = -\nabla p + \rho \boldsymbol{g} + \mu \nabla^2 \boldsymbol{v} \quad . \tag{2.1}$$

Here, flow with velocity $\boldsymbol{v}$ and incompressible Newtonian fluid with a constant viscosity μ is considered. The left side of the equation contains inertial terms where ρ is density and the inside of the parenthesis corresponds to the acceleration of the fluid

$$\rho \boldsymbol{a} = \rho(\frac{\partial \boldsymbol{v}}{\partial t} + (\nabla \boldsymbol{v})\boldsymbol{v}) \quad . \tag{2.2}$$

On the right side of the (2.1), p is the pressure and $\boldsymbol{g}$ is the body force per unit mass. Thin film lubrication setup imposes a small characteristic length scale in the present work. This renders the viscous terms dominant over the inertial terms. Therefore, inertial terms on the left hand side and the body force on the right hand side can be eliminated, which leaves (2.1) in a simplified form, namely the Stokes equation:

$$0 = -\nabla p + \mu \nabla^2 \boldsymbol{v} \quad . \tag{2.3}$$

Note that, alternatively this simplification also emerges from the non-dimensional form of the Navier-Stokes equation. Here, the Reynolds number naturally appears and indicates insignificant inertial terms when compared with viscous forces [4].

Due to small film thickness, changes in the normal direction for pressure can be omitted so that $p = p(x_1, x_2)$. In view of the further simplifications due to thin film assumption, (2.3) further reduces to the following form for lateral directions [4]

$$\frac{\partial p}{\mathrm{d}x_1} = \mu\frac{\partial^2 v_1}{\mathrm{d}x_3^2} \qquad \frac{\partial p}{\mathrm{d}x_2} = \mu\frac{\partial^2 v_2}{\mathrm{d}x_3^2} \quad . \tag{2.4}$$

The solution of this system takes the form:

$$\begin{aligned} v_1 &= \frac{\partial p}{\partial x_1}\frac{x_3^2}{2\mu} + Ax_3 + B \\ v_2 &= \frac{\partial p}{\partial x_2}\frac{x_3^2}{2\mu} + Cx_3 + D \quad . \end{aligned} \tag{2.5}$$

There are four boundary conditions to find the unknown coefficients which are implemented at upper and lower surfaces as velocities $U_i^{\pm}$

$$\begin{aligned} x_3 = 0 : &\qquad v_1 = U_1^-, v_2 = U_2^- \\ x_3 = h : &\qquad v_1 = U_1^+, v_2 = U_2^+ \quad . \end{aligned} \tag{2.6}$$

These boundary conditions make the solution of the Stokes equation as follows:

$$\begin{aligned} v_1 &= \frac{\partial p}{\partial x_1}\frac{x_3^2}{2\mu} + (\frac{U_1^+ - U_1^-}{h} - \frac{\partial p}{\partial x_1}\frac{h}{2\mu})x_3 + U_1^- \\ v_2 &= \frac{\partial p}{\partial x_2}\frac{x_3^2}{2\mu} + (\frac{U_2^+ - U_2^-}{h} - \frac{\partial p}{\partial x_2}\frac{h}{2\mu})x_3 + U_2^- \quad . \end{aligned} \tag{2.7}$$

Subsequently, integration over x_3 is applied to the velocities to determine the flux in the two lateral directions:

$$\begin{aligned} q_1 &= -\frac{\partial p}{\partial x_1}\frac{h^3}{12\mu} + \frac{(U_1^+ + U_1^-)h}{2} \\ q_2 &= -\frac{\partial p}{\partial x_2}\frac{h^3}{12\mu} + \frac{(U_2^+ + U_2^-)h}{2} \quad . \end{aligned} \tag{2.8}$$

Here, summation of the surface velocities is defined as $\boldsymbol{U} = \boldsymbol{U}^+ + \boldsymbol{U}^-$. At this stage, continuity equation is added as a third equation to (2.4) which indicates the fluid coming inside of a unit volume is set equal to the fluid leaving the unit volume

$$\frac{\partial \rho}{\partial t} + \nabla \cdot (\rho \boldsymbol{v}) = 0 \quad . \tag{2.9}$$

Noting that the fluid is taken to be incompressible and the density of the fluid is considered to be constant everywhere, continuity equation simplifies to the following form:

$$\nabla \cdot \boldsymbol{v} = \frac{\partial v_1}{\partial x_1} + \frac{\partial v_2}{\partial x_2} + \frac{\partial v_3}{\partial x_3} = 0 \quad . \tag{2.10}$$

Rearranging (2.10) and taking integral over the normal direction, continuity equation leads to

$$\int_0^h \frac{\partial v_1}{\partial x_1} dx_3 + \int_0^h \frac{\partial v_2}{\partial x_2} dx_3 = -\int_0^h \frac{\partial v_3}{\partial x_3} dx_3 \quad . \tag{2.11}$$

The left-hand side of this equation can be rewritten as the divergence of the flux by using (2.8) and performing integration before the derivatives. On the other hand, for the unknown term v_3, the derivative can be expressed in terms of normal fluid velocities at the surfaces:

$$v_3^+ - v_3^- = \frac{\partial h}{\partial t} \quad . \tag{2.12}$$

This relation makes the right hand side of (2.11) equal to the difference of the normal velocities, which corresponds to the average speed of the film thickness. Therefore the continuity equation leads to

$$-\left(\frac{\partial q_1}{\partial x_1} + \frac{\partial q_2}{\partial x_2}\right) = \frac{\partial h}{\partial t} \quad . \tag{2.13}$$

Finally, using the open form of fluxes from (2.8), Reynolds equation is obtained as

$$-\boldsymbol{\nabla \cdot} (\boldsymbol{q}) = \frac{\partial h}{\partial t} \tag{2.14}$$

where

$$\boldsymbol{q} = -\frac{h^3}{12\mu} \nabla \boldsymbol{p} + \frac{h}{2} \boldsymbol{U} \quad . \tag{2.15}$$

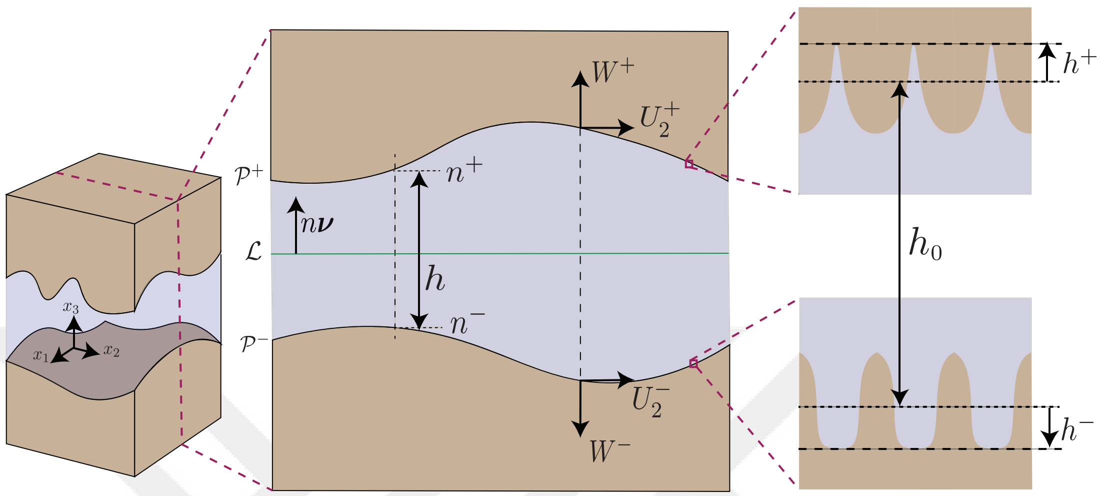

Figure 2.1: *Multiscale lubrication interface is illustrated.*

Additional to the flux, traction at the surfaces is also used later in the optimization scheme. The total traction that needs to be applied for equilibriation at the upper and the lower surface is indicated as $\boldsymbol{t}^{\pm}$ following Cakal et al. [35]. This traction consists of normal and tangential counterparts as

$$\boldsymbol{t}^{\pm} = \mp p\boldsymbol{v} + \boldsymbol{\tau}^{\pm} \quad . \tag{2.16}$$

Here $\boldsymbol{\nu}$ indicates the unit vector which is normal to the lubrication surface $\mathcal{L}$, and $n^{\pm}$ indicates the distances from $\mathcal{L}$ to the upper and lower surfaces $\mathcal{P}^{\pm}$ respectively. This is demonstrated in Figure 2.1. Here, the tangential traction can be decomposed into two terms [4]

$$\boldsymbol{\tau}^{\pm} = \boldsymbol{\tau}_p^{\pm} + \boldsymbol{\tau}_v^{\pm}. \tag{2.17}$$

The first term occurs since the non-conformal surfaces change fluid thickness as they move, namely

$$\boldsymbol{\tau}_p^{\pm} = \pm p \nabla n^{\pm}, \tag{2.18}$$

and the second one occurs due to viscous flow:

$$\boldsymbol{\tau}_v^{\pm} = \frac{h}{2}\boldsymbol{g} \pm \frac{\mu}{h}\boldsymbol{V} \quad . \tag{2.19}$$

Chapter 3

Homogenization and Sensitivity Analysis

In this chapter, the homogenization of the Reynolds equation is obtained for the case of unilateral roughness. Subsequently, analytical sensitivities of the texture parameters are derived for the homogenized system.

3.1 Homogenization of Reynolds Equation

In order to analyze the micro-texture dependence on the macroscopic response of the fluid at the interface, homogenization of the Reynolds equation is carried out. Pressure and the film thickness fluctuate rapidly as a function of macroscopic space-time which leads to an oscillatory response. The oscillatory quantities are absolute space and time. These are shown with the subscript ϵ in the Reynolds equation:

$$-\nabla_{\boldsymbol{x}_\epsilon} \cdot \left(-\frac{h_\epsilon^3(\boldsymbol{x}_\epsilon, t_\epsilon)}{12\mu} \nabla_{\boldsymbol{x}_\epsilon} p_\epsilon(\boldsymbol{x}_\epsilon, t_\epsilon) + \frac{h_\epsilon(\boldsymbol{x}_\epsilon, t_\epsilon)}{2} \boldsymbol{U} \right) = \frac{\partial h_\epsilon(\boldsymbol{x}_\epsilon, t_\epsilon)}{\partial t} \quad . \tag{3.1}$$

In this work, motion of the active texture is in the normal direction and accepted to have only macroscopic time dependency. Therefore time parameter is eliminated from the micro-scale dependencies by setting $t_\epsilon = t(\boldsymbol{x})$. On the other hand, for position a two-scale separation is applied to differentiate between microscopic and macroscopic scales

$$\boldsymbol{x}_\epsilon = \boldsymbol{x} + \epsilon \boldsymbol{y}. \tag{3.2}$$

Here, $\boldsymbol{x}_\epsilon$ is the absolute position that is separated into macroscopic $\boldsymbol{x}$ and microscopic $\boldsymbol{y}$ counterparts with $\epsilon \ll 1$. As a consequence of the scale separation, the derivative operator may be expressed as

$$\nabla_{\boldsymbol{x}_\epsilon} = \nabla_{\boldsymbol{x}} + \epsilon^{-1} \nabla_{\boldsymbol{y}} \quad . \tag{3.3}$$

Subsequently, the film thickness and the pressure are written in terms of these separated parameters. The film thickness takes the form

$$h_\epsilon(\boldsymbol{x}_\epsilon, t) = h(\boldsymbol{x}, \boldsymbol{y}, t) = h_0(\boldsymbol{x}, t) + h^+(\boldsymbol{y}, t) - h^-(\boldsymbol{y}, t) \tag{3.4}$$

where h_0 is the smooth macroscopic variation and h^+ and h^- show the microscopic change as depicted in Figure 2.1. In this study, unilateral roughness setting is considered where upper texture is smooth as shown in Figure 3.1 and since h^+ is eliminated in the set up, h^- is simply denoted as $\bar{h}$. Moreover, h_o is considered as a constant in the optimization scheme where the average of $\bar{h}$ is set to zero over the spatial microscopic domain. Therefore, the right-hand side of the Reynolds equation effectively leads to zero and the film thickness is simply demonstrated as $h = h_0 - \bar{h}$.

In order to invoke the homogenization process, the absolute pressure is separated into macroscopic pressure term p_0 and microscopic corrector terms p_i , $i = 1, 2, ..$ via asymptotic expansion,

$$p_\epsilon = p_0(\boldsymbol{x}, \boldsymbol{y}, t) + \epsilon p_1(\boldsymbol{x}, \boldsymbol{y}, t) + \epsilon^2 p_2(\boldsymbol{x}, \boldsymbol{y}, t) + \mathcal{O}(\epsilon^3), \tag{3.5}$$

which updates Reynolds Equation towards the form

$$-(\nabla_{\boldsymbol{x}} + \epsilon^{-1} \nabla_{\boldsymbol{y}}) \cdot \left(-\frac{h^3}{12\mu} (\nabla_{\boldsymbol{x}} + \epsilon^{-1} \nabla_{\boldsymbol{y}})(p_0 + \epsilon p_1 + \epsilon^2 p_2) + \frac{h}{2} \boldsymbol{U} \right) = 0 \quad . \tag{3.6}$$

Carrying out the operations, and defining coefficients as $a = \frac{h^3}{12\mu}$, $b = \frac{h}{2}$, parameters are grouped according to orders

$$\epsilon^{-2}(A_0 p_0(\boldsymbol{x}, \boldsymbol{y}, t)) = 0 \tag{3.7a}$$

$$\epsilon^{-1}(A_1 p_0 + A_0 p_1) = \nabla_{\boldsymbol{y}} \cdot (b\boldsymbol{U}) \tag{3.7b}$$

$$\epsilon^{0}(A_2 p_0 + A_1 p_1 + A_0 p_2) = \nabla_{\boldsymbol{x}} \cdot (b\boldsymbol{U}), \tag{3.7c}$$

where the operators are defined as:

$$A_0 = \nabla_{\boldsymbol{y}} \cdot a \nabla_{\boldsymbol{y}} \tag{3.8a}$$

$$A_1 = \nabla_{\boldsymbol{x}} \cdot a \nabla_{\boldsymbol{y}} + \nabla_{\boldsymbol{y}} \cdot a \nabla_{\boldsymbol{x}} \tag{3.8b}$$

$$A_2 = \nabla_{\boldsymbol{x}} \cdot a \nabla_{\boldsymbol{x}} \quad . \tag{3.8c}$$

From (3.7a), one can see that p_0 is independent of microscale position $\boldsymbol{y}$, i.e. $p_0 = p_0(\boldsymbol{x}, t)$. Therefore the first term on the right hand side of (3.7b) is eliminated. Reordering (3.7b) with remaining terms with the aim of finding a form for p_1 delivers

$$\nabla_{\boldsymbol{y}} \cdot a \nabla_{\boldsymbol{y}} p_1 = -\nabla_{\boldsymbol{y}} \cdot a \nabla_{\boldsymbol{x}} p_0 + \nabla_{\boldsymbol{y}} \cdot b\boldsymbol{U} \quad . \tag{3.9}$$

Here, $p_i(\boldsymbol{x}, \boldsymbol{y}), i \in 1, 2$ are periodic in microscale domain $\mathcal{Y}$ with $\boldsymbol{y}$. Therefore for p_1 to have a solution, the right hand side of (3.9) should be periodic as well and satisfy

$$\langle -\nabla_{\boldsymbol{y}} \cdot a \nabla_{\boldsymbol{x}} p_0 + \nabla_{\boldsymbol{y}} \cdot b\boldsymbol{U} \rangle = 0 \tag{3.10}$$

where $\langle \mathcal{Q} \rangle = |\mathcal{Y}|^{-1} \int_{\mathcal{Y}} \mathcal{Q} \, \mathrm{d}v$. Noticing that the pressure gradient and the velocity are independent of the microscopic variations in (3.10), separation of variables is used to propose a solution

$$p_1 = \boldsymbol{G}(\boldsymbol{x})\boldsymbol{\omega}(\boldsymbol{y}) - \boldsymbol{V}(\boldsymbol{x})\boldsymbol{\Omega}(\boldsymbol{y}) \tag{3.11}$$

where $\boldsymbol{G} = \nabla_{\boldsymbol{x}} p_0$ is macroscopic pressure gradient and $\boldsymbol{V} = \boldsymbol{U}^+ - \boldsymbol{U}^-$ is the relative velocity. The periodic fields $\boldsymbol{\omega}$ and $\boldsymbol{\Omega}$ are called first order correctors and satisfy the solvability condition (3.10). Substituting the proposed solution for p_1 in (3.9), one obtains

$$\nabla_{\boldsymbol{y}} \cdot a \nabla_{\boldsymbol{y}} (\boldsymbol{G}\boldsymbol{\omega} - \boldsymbol{V}\boldsymbol{\Omega}) = -\nabla_{\boldsymbol{y}} \cdot (a\boldsymbol{G}) + \nabla_{\boldsymbol{y}} \cdot (b\boldsymbol{U}) \quad . \tag{3.12}$$

This equation can now be regrouped into two sets of equations called cell problems by noticing that macroscopic pressure gradient and velocities are independent of the microscale. By simplifying with respect to pressure gradient and velocity, cell problems take the form

$$\nabla_{\boldsymbol{y}} \cdot a \nabla_{\boldsymbol{y}} \boldsymbol{\omega} = -\nabla_{\boldsymbol{y}} a \tag{3.13a}$$

$$\nabla_{\boldsymbol{y}} \cdot a \nabla_{\boldsymbol{y}} \boldsymbol{\Omega} = -\nabla_{\boldsymbol{y}} b \quad . \tag{3.13b}$$

Note that since the unilateral setting is adopted, only the upper surface has a non-zero lateral velocity; therefore $\boldsymbol{U} = \boldsymbol{V} = \boldsymbol{U}^+$. Also, for a system that considers the change in microscopic time due to roughness of both surfaces, one may refer to the study [50]. In such a scenario, cell problems would have additional terms that shows the change of film thickness with respect to microscopic time which result in fluctuating homogenized tensors with respect to microscopic time scale.

Now considering equation 3.7c, it is rewritten in the alternative form

$$A_0 p_2 = -A_2 p_0 - A_1 p_1 + \nabla_{\boldsymbol{x}} \cdot (b\boldsymbol{U}) \tag{3.14}$$

in which the averaging of the right hand side over $\mathcal{Y}$ should be zero again for p_2 to have a solution

$$\langle -A_2 p_0 - A_1 p_1 + \nabla_{\boldsymbol{x}} \cdot (b\boldsymbol{U}) \rangle = 0 \quad . \tag{3.15}$$

This solvability condition implies

$$\langle A_2 p_0 + A_1 p_1 \rangle = \nabla_{\boldsymbol{x}} \cdot (\langle b \rangle \boldsymbol{U}) \tag{3.16}$$

since the right hand side is independent of $\boldsymbol{y}$ over the unit micro domain. First term on the left hand side leads to

$$\begin{aligned} \langle A_2 p_0 \rangle =& \langle \nabla_{\boldsymbol{x}} \cdot a(\boldsymbol{y}) \nabla_{\boldsymbol{x}} p_0 \rangle \\ =& \nabla_{\boldsymbol{x}} \cdot [\langle a(\boldsymbol{y}) \rangle G], \end{aligned} \tag{3.17}$$

and the second term delivers

$$\begin{aligned} \langle A_1 p_1 \rangle =& \langle \nabla_{\boldsymbol{y}} \cdot a(\boldsymbol{y}) \nabla_{\boldsymbol{x}} p_1 + \nabla_{\boldsymbol{x}} \cdot a(\boldsymbol{y}) \nabla_{\boldsymbol{y}} p_1 \rangle \\ =& \nabla_{\boldsymbol{x}} \cdot [(\langle a(\boldsymbol{y}) \nabla_{\boldsymbol{y}} p_1 \rangle)] \\ =& \nabla_{\boldsymbol{x}} \cdot [\langle a(\boldsymbol{y}) \nabla_{\boldsymbol{y}} \boldsymbol{\omega} \rangle \boldsymbol{G} - \langle a(\boldsymbol{y}) \nabla_{\boldsymbol{y}} \boldsymbol{\Omega} \rangle \boldsymbol{U}] \quad . \end{aligned} \tag{3.18}$$

The term $\langle -\nabla_{\boldsymbol{y}} \cdot a(\boldsymbol{y})\nabla_{\boldsymbol{x}} p_1 \rangle$ in (3.18) vanishes due to periodicity. Plugging (3.17) and (3.18) in (3.16), homogenized the Reynolds equation is obtained:

$$-\nabla_{\boldsymbol{x}} \cdot [-\langle a + a\nabla_{\boldsymbol{y}}\boldsymbol{\omega}\rangle \boldsymbol{G} + \langle a\nabla_{\boldsymbol{y}}\boldsymbol{\Omega}\rangle \boldsymbol{U} + \langle b\rangle \boldsymbol{U}] = 0 \tag{3.19}$$

At this point, a more compact notation is adapted for the gradient of the corrector terms by eliminating the sub letter $\boldsymbol{y}$:

$$\nabla\boldsymbol{\omega} = \boldsymbol{\lambda} \qquad \nabla\boldsymbol{\Omega} = \boldsymbol{\Lambda}. \tag{3.20}$$

Explicitly, in terms of indices

$$\frac{\partial \omega_i}{\partial y_j} = \lambda^i_j \qquad \frac{\partial \Omega_i}{\partial y_j} = \Lambda^i_j \quad . \tag{3.21}$$

Finally, *flow factor* tensors $\boldsymbol{A}$ and $\boldsymbol{B}$ are defined and similarly put in a compact form

$$\boldsymbol{A} = \left\langle a\boldsymbol{I} + a\boldsymbol{\lambda}^T \right\rangle = \left\langle a\boldsymbol{\Gamma}^T \right\rangle \tag{3.22a}$$

$$\boldsymbol{C} = \left\langle b\boldsymbol{I} + a\boldsymbol{\Lambda}^T \right\rangle = \left\langle \boldsymbol{\Phi}^T \right\rangle, \tag{3.22b}$$

so that flux takes the form

$$\boldsymbol{Q} = -\boldsymbol{A}\boldsymbol{G} + \boldsymbol{B}\boldsymbol{V} \quad . \tag{3.23}$$

Additional to flux, traction is also written in terms of homogenized quantities. In this regard, microscale traction in (2.16) is written in terms of macroscopic counterparts by avaraging

$$\begin{aligned} \boldsymbol{T}^{\pm} &= \langle \pm p_\epsilon \boldsymbol{v}\rangle + \left\langle \boldsymbol{\tau}^{\pm}_{\epsilon} \right\rangle \\ &= p_0 \boldsymbol{v} + \boldsymbol{\mathcal{T}}^{\pm} \quad . \end{aligned} \tag{3.24}$$

Following a similar analysis as before, traction due to fluid can be separated in two parts

$$\boldsymbol{\mathcal{T}}^{\pm} = \boldsymbol{\mathcal{T}}^{\pm}_p + \boldsymbol{\mathcal{T}}^{\pm}_\nu \tag{3.25}$$

where $\boldsymbol{\mathcal{T}}^{\pm}_p$ is the tangential component and $\boldsymbol{\mathcal{T}}^{\pm}_\nu$ is the shear component. To conduct the analysis, out of plane position for $n^{\pm}$ is rewritten for the unilateral setting

$$n^{\pm}_{\epsilon} = n^{\pm}_0(\boldsymbol{x}, t) + h^{\pm}(\boldsymbol{y}, t) \quad . \tag{3.26}$$

Here, n^+ and related positive variations are eliminated due to unilateral setting where lubrication surface coincides with the upper surface $\mathcal{P}^+$. Moreover, $\langle h^- \rangle = \langle \bar{h} \rangle = 0$ is enforced; therefore the tangential term (2.18) leads to:

$$\begin{aligned}
\mathcal{T}_p^{\pm} &= \pm \left\langle p_\epsilon \nabla n_\epsilon^{\pm} \right\rangle \\
&= \pm(p_0 + \epsilon p_1 + \epsilon^2 p_2)((\nabla_{\boldsymbol{x}} + \epsilon^{-1}\nabla_{\boldsymbol{y}})n_\epsilon^{\pm}) \\
&= \pm(p_0 \nabla_{\boldsymbol{x}} n_\epsilon^{\pm} + p_1 \nabla_{\boldsymbol{y}} n_\epsilon^{\pm}) \\
&= \pm(p_0 \nabla_{\boldsymbol{x}} n_0^{\pm} + p_1 \nabla_{\boldsymbol{y}} h^{\pm}) \\
&= \pm p_0 \nabla_{\boldsymbol{x}} n_0^{\pm} \pm (\left\langle h^{\pm} \nabla_{\boldsymbol{y}} \omega \right\rangle \boldsymbol{G} \mp \left\langle h^{\pm} \nabla_{\boldsymbol{y}} \Omega \right\rangle \boldsymbol{V}) \\
&= \pm p_0 \nabla_{\boldsymbol{x}} n_0^{\pm} \pm \left\langle h^{\pm} \boldsymbol{\lambda}^T \right\rangle \boldsymbol{G} \mp \left\langle h^{\pm} \boldsymbol{\Lambda}^T \right\rangle \boldsymbol{V} \quad .
\end{aligned} \tag{3.27}$$

Defining $e = \frac{\mu}{h}$, the viscous term (2.19) for is updated in a similar manner one obtains

$$\begin{aligned}
\mathcal{T}_\nu^{\pm} &= \langle b \nabla p_\epsilon \pm e \boldsymbol{V} \rangle \\
&= \left\langle b(\nabla_{\boldsymbol{x}} + \epsilon^{-1} \nabla_{\boldsymbol{y}})(p_0 + \epsilon p_1 + \epsilon^2 p_2) \pm e \boldsymbol{V} \right\rangle \\
&= \langle b(\nabla_{\boldsymbol{x}} p_0 + \nabla_{\boldsymbol{y}} p_1) \pm e \boldsymbol{V} \rangle \\
&= \langle b(\nabla_{\boldsymbol{x}} p_0 + (\nabla_{\boldsymbol{y}} \omega \boldsymbol{G} - \nabla_{\boldsymbol{y}} \Omega \boldsymbol{V})) \pm e \boldsymbol{V} \rangle \\
&= \langle b \boldsymbol{I} + b \nabla_{\boldsymbol{y}} \omega \rangle \boldsymbol{G} \pm \langle e \boldsymbol{I} \mp b \nabla_{\boldsymbol{y}} \boldsymbol{\Lambda} \rangle \boldsymbol{V} \\
&= \left\langle b \boldsymbol{I} + b \boldsymbol{\lambda}^T \right\rangle \boldsymbol{G} \pm \left\langle e \boldsymbol{I} \mp b \boldsymbol{\Lambda}^T \right\rangle \boldsymbol{V} \quad .
\end{aligned} \tag{3.28}$$

In the present setting n_0 is preserved and spatial average of h is adjusted to be zero, therefore only $\mathcal{T}_\nu$ survives. Also, due to unilateral setup, only $\mathcal{T}_\nu^+$ is needed. Renaming $\mathcal{T}_\nu^+ = \overline{\mathcal{T}}$ and defining the *stress factor* tensors as

$$\boldsymbol{D} = \left\langle b \boldsymbol{I} + b \boldsymbol{\lambda}^T \right\rangle \tag{3.29a}$$

$$\boldsymbol{F} = \left\langle e \boldsymbol{I} - b \boldsymbol{\Lambda}^T \right\rangle , \tag{3.29b}$$

so that the macroscopic traction takes the form

$$\overline{\boldsymbol{\mathcal{T}}} = \boldsymbol{D}\boldsymbol{G} + \boldsymbol{F}\overline{\boldsymbol{U}} \quad . \tag{3.30}$$

It can readily be shown that $\boldsymbol{D} = \boldsymbol{C}^T$ [35]. The forms obtained for flux in (3.23) and traction in (3.30) are later used in the optimization scheme where the homogenized coefficients are calculated on a discretized unit domain introduced in Chapter 4.

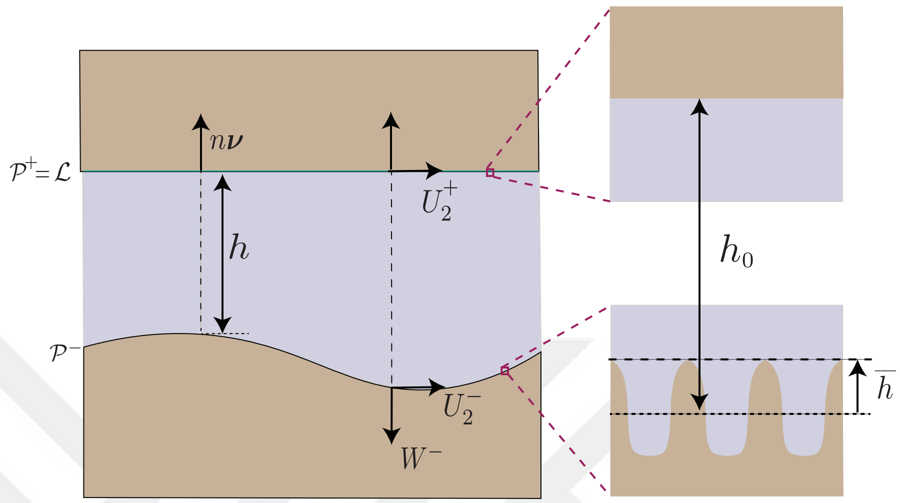

Figure 3.1: *Unilateral lubrication interface is demonstrated.*

3.2 Sensitivity Analysis

For the flux and traction optimization schemes, sensitivity of the coefficient tensors are introduced in this section. Sensitivities are divided into two categories: film thickness variable and geometry variable sensitivities. The first one indicates the dependence of the tensors to the distribution and time dependent change of the film thickness, whereas the second indicates dependence of the tensors to the unit cell shape. Tensor $\boldsymbol{D}$ is not separately considered in the following discussions since it is the transpose of $\boldsymbol{C}$.

3.2.1 Film Thickness Variable Sensitivity

Tensorial quantities $\boldsymbol{A}$, $\boldsymbol{C}$ and $\boldsymbol{F}$ depend on the distribution of the film thickness over the unit domain. At this point, it is assumed that the film thickness may be written as a function of a generic design variable ζ which may be associated with either the spatial or temporal distribution of $h(\boldsymbol{y}, t)$. In order to obtain relevant sensitivities, cell problems in (3.13) are written with their compact notations

$$\nabla \cdot (a\boldsymbol{I} + a\boldsymbol{\lambda}) = \nabla \cdot (a\boldsymbol{\Gamma}) = \boldsymbol{0} \tag{3.31a}$$

$$\nabla \cdot (b\boldsymbol{I} + a\boldsymbol{\Lambda}) = \nabla \cdot (\boldsymbol{\Phi}) = \boldsymbol{0} \tag{3.31b}$$

which define the tensors $\boldsymbol{\Gamma}$ and $\boldsymbol{\Phi}$. These cell problems are written in the weak form for the variational formulation

$$\langle a\boldsymbol{\Gamma}\nabla\eta\rangle = \boldsymbol{0} \tag{3.32a}$$

$$\langle \boldsymbol{\Phi}\nabla\theta\rangle = \boldsymbol{0}, \tag{3.32b}$$

where η and θ are periodic test functions. Suitable periodic functions will be assigned to these test functions throughout the subsequent derivations. First, in order to derive alternative expressions of $\boldsymbol{A}$ and $\boldsymbol{B}$ vector field ω_i is prescribed to both η and θ and the following forms are obtained:

$$\left\langle a\boldsymbol{\Gamma}(\nabla\boldsymbol{\omega})^T\right\rangle = \left\langle a\boldsymbol{\Gamma}\boldsymbol{\lambda}^T\right\rangle = \boldsymbol{0} \tag{3.33a}$$

$$\left\langle \boldsymbol{\Phi}(\nabla\boldsymbol{\omega})^T\right\rangle = \left\langle \boldsymbol{\Phi}\boldsymbol{\lambda}^T\right\rangle = \boldsymbol{0} \quad . \tag{3.33b}$$

These forms are added to the vanishing integrals in (3.22) respectively. For $\boldsymbol{A}$, the transpose of (3.33a) is added to (3.22a) which delivers

$$\boldsymbol{A} = \left\langle a\boldsymbol{\Gamma}^T\right\rangle + \left\langle a\boldsymbol{\lambda}\boldsymbol{\Gamma}^T\right\rangle = \left\langle \boldsymbol{\Gamma}a\boldsymbol{\Gamma}^T\right\rangle \quad . \tag{3.34}$$

Similarly for $\boldsymbol{C}$, the transpose of (3.33b) is added to (3.22b)

$$\boldsymbol{C} = \left\langle \boldsymbol{\Phi}^T\right\rangle + \left\langle \boldsymbol{\lambda}\boldsymbol{\Phi}^T\right\rangle = \left\langle \boldsymbol{\Gamma}\boldsymbol{\Phi}^T\right\rangle \quad . \tag{3.35}$$

In addition, $\boldsymbol{F}$ is also expressed alternatively by adding the transpose of (3.32b) to (3.29b) where θ is chosen as Ω_i in (3.33b):

$$\begin{aligned}\boldsymbol{F} &= \left\langle e\boldsymbol{I} - b\boldsymbol{\Lambda}^T\right\rangle + \left\langle \boldsymbol{\Phi}(\nabla)^T\right\rangle \\ &= \left\langle e\boldsymbol{I} - b\boldsymbol{\Lambda}^T + (b\boldsymbol{I} + a\boldsymbol{\Lambda})\boldsymbol{\Lambda}^T\right\rangle \\ &= \left\langle e\boldsymbol{I} + a\boldsymbol{\Lambda}\boldsymbol{\Lambda}^T\right\rangle \quad .\end{aligned} \tag{3.36}$$

Now, using these forms, the sensitivity of $\boldsymbol{A}$ with respect to ζ may be written:

$$\frac{\partial \boldsymbol{A}}{\partial\zeta} = \left\langle \frac{\partial\boldsymbol{\Gamma}}{\partial\zeta}a\boldsymbol{\Gamma}^T\right\rangle + \left\langle \boldsymbol{\Gamma}\frac{\partial a}{\partial\zeta}\boldsymbol{\Gamma}^T\right\rangle + \left\langle \boldsymbol{\Gamma}a\frac{\partial\boldsymbol{\Gamma}^T}{\partial\zeta}\right\rangle . \tag{3.37}$$

Here, the first and the third term average to zero since they become equal to the vanishing integral in (3.33a) when the test function η is chosen as $\frac{\partial \omega_i}{\partial \zeta}$. Therefore sensitivity of $\boldsymbol{A}$ with respect to ζ takes the form

$$\frac{\partial \boldsymbol{A}}{\partial \zeta} = \left\langle \boldsymbol{\Gamma} \frac{\partial a}{\partial \zeta} \boldsymbol{\Gamma}^T \right\rangle \tag{3.38}$$

where ζ controls film thickness h through a. Similarly, the derivative of $\boldsymbol{C}$ follows

$$\begin{aligned} \frac{\partial \boldsymbol{C}}{\partial \zeta} &= \left\langle \frac{\partial \boldsymbol{\Gamma}}{\partial \zeta} \boldsymbol{\Phi}^T \right\rangle + \left\langle \boldsymbol{\Gamma} \frac{\partial \boldsymbol{\Phi}^T}{\partial \zeta} \right\rangle \\ &= \left\langle \frac{\partial \boldsymbol{\lambda}}{\partial \zeta} \boldsymbol{\Phi}^T \right\rangle + \left\langle \boldsymbol{\Gamma} \frac{\partial b}{\partial \zeta} \boldsymbol{I} \right\rangle + \left\langle \boldsymbol{\Gamma} \frac{\partial a}{\partial \zeta} \boldsymbol{\lambda}^T \right\rangle + \left\langle \boldsymbol{\Gamma} a \frac{\partial \boldsymbol{\lambda}^T}{\partial \zeta} \right\rangle \quad . \end{aligned} \tag{3.39}$$

In the expanded form above, first term vanishes upon choosing $\theta = \frac{\partial \omega_i}{\partial \zeta}$, and the fourth term is vanishes upon choosing $\theta = \frac{\partial \Omega_i}{\partial \zeta}$ in (3.32b). Therefore the sensitivity of $\boldsymbol{C}$ with respect to ζ delivers

$$\frac{\partial \boldsymbol{C}}{\partial \zeta} = \left\langle \boldsymbol{\Gamma} (\frac{\partial b}{\partial \zeta} \boldsymbol{I} + \frac{\partial a}{\partial \zeta} \boldsymbol{\Lambda}^T) \right\rangle \quad . \tag{3.40}$$

For $\boldsymbol{F}$, expression in (3.36) is used to take the sensitivity with respect to ζ

$$\frac{\partial \boldsymbol{F}}{\partial \zeta} = \left\langle \frac{\partial e}{\partial \zeta} \boldsymbol{I} + \frac{\partial a}{\partial \zeta} \boldsymbol{\Lambda} \boldsymbol{\Lambda}^T + a \frac{\partial \boldsymbol{\Lambda}}{\partial \zeta} \boldsymbol{\Lambda}^T + a \boldsymbol{\Lambda} \frac{\partial \boldsymbol{\Lambda}^T}{\partial \zeta} \right\rangle \quad . \tag{3.41}$$

In order to simplify this expression, a useful relation is employed using (3.32b) upon replacing $\boldsymbol{\Phi}$ with $\frac{\partial \boldsymbol{\Phi}}{\partial \zeta}$ and θ with Ω_i :

$$\left\langle a \frac{\partial \boldsymbol{\Lambda}}{\partial \zeta} \boldsymbol{\Lambda}_T \right\rangle = - \left\langle \frac{\partial b}{\partial \zeta} \boldsymbol{\Lambda}^T + \frac{\partial a}{\partial \zeta} \boldsymbol{\Lambda} \boldsymbol{\Lambda}^T \right\rangle \quad . \tag{3.42}$$

Replacing this expression with the third term in (3.41) and the transpose of this expression with the fourth term in (3.41), sensitivity of $\boldsymbol{F}$ with respect to ζ is finally obtained:

$$\frac{\partial \boldsymbol{F}}{\partial \zeta} = \left\langle \frac{\partial e}{\partial \zeta} \boldsymbol{I} - \frac{\partial b}{\partial \zeta} (\boldsymbol{\Lambda} + \boldsymbol{\Lambda}^T) - \frac{\partial a}{\partial \zeta} \boldsymbol{\Lambda} \boldsymbol{\Lambda}^T \right\rangle \quad . \tag{3.43}$$

Note that the sensitivity of $\boldsymbol{A}$ takes a form that is reminiscent of heat conduction or elasticity problem [47], on the other hand $\boldsymbol{C}$ is not symmetric in general. In the final expressions for the film thickness sensitivities, all expressions have derivatives with respect to coefficients a, b and e with which the film thickness is directly related. The explicit form for the sensitivities of these coefficients with respect to design variables, which are represented by ζ so far, are given in Chapter 5.

3.2.2 Geometry Variable Sensitivity

It has been shown that working on a fixed domain during the optimization can cause restricted design space and therefore suboptimal results [35, 53]. As demonstrated in [53], by adapting the shape of the unit cell, the design space can be expanded. Therefore by changing the unit cell shape, optimization will have an improved flexibility towards optimality. In order to control the shape of the unit cell, referential position $\boldsymbol{y}_0$ is subjected a linear transformation $\boldsymbol{y} = \boldsymbol{P}\boldsymbol{y}_0$ where the components of $\boldsymbol{P}$ are controlled by a design variable γ. In this section, the derivation of the sensitivities for homogenized coefficients $\boldsymbol{A}$, $\boldsymbol{C}$ and $\boldsymbol{F}$ with respect to γ is presented. For the domain average of the quantities, notation $\langle \mathcal{Q} \rangle_o = |\mathcal{Y}_o|^{-1} \int_{\mathcal{Y}_o} \mathcal{Q} \, \mathrm{d}v_o$ is used following [53]. Due to applied linear transformation, domain average in the referential configuration is equal to the domain avarage in the current configuration: $\langle \mathcal{Q} \rangle_o = \langle \mathcal{Q} \rangle$. Starting with the tensor $\boldsymbol{A}$, derivative with respect to γ is taken

$$\frac{\partial \boldsymbol{A}}{\partial \gamma} = \frac{\partial}{\partial \gamma} \left\langle \boldsymbol{\Gamma} \, a \, \boldsymbol{\Gamma}^T \right\rangle_o \quad . \tag{3.44}$$

Note that coefficients a, b and e and their distribution due to film thickness is not affected from the changes in the unit cell. Adding further definitions $\nabla_o = \frac{\partial}{\partial \boldsymbol{y}_o}$ and $\boldsymbol{M} = \boldsymbol{P}^{-1}$, the corrector field gradient is decomposed

$$\boldsymbol{\Upsilon} = \nabla_o \boldsymbol{\omega} \tag{3.45a}$$

$$\boldsymbol{\lambda} = \boldsymbol{\Upsilon} \boldsymbol{M} \quad . \tag{3.45b}$$

Distributing the derivative and noticing that $\frac{\partial \boldsymbol{\Gamma}}{\partial \gamma} = \frac{\partial \boldsymbol{\lambda}}{\partial \gamma}$, (3.44) delivers

$$\begin{aligned} \frac{\partial \boldsymbol{A}}{\partial \gamma} &= \left\langle \frac{\partial (\boldsymbol{\Upsilon}\boldsymbol{M})}{\partial \gamma} \, a \, \boldsymbol{\Gamma}^T \right\rangle_o + \left\langle \boldsymbol{\Gamma} \, a \, \frac{\partial (\boldsymbol{\Upsilon}\boldsymbol{M})^T}{\partial \gamma} \right\rangle_o \\ &= \left\langle a \frac{\partial \boldsymbol{\Upsilon}}{\partial \gamma} \boldsymbol{M} \boldsymbol{\Gamma}^T \right\rangle_o + \left\langle a \boldsymbol{\Upsilon} \frac{\partial \boldsymbol{M}}{\partial \gamma} \boldsymbol{\Gamma}^T \right\rangle_o + \left\langle a \boldsymbol{\Gamma}^T \frac{\partial \boldsymbol{\Upsilon}^T}{\partial \gamma} \boldsymbol{M} \right\rangle_o + \left\langle a \boldsymbol{\Gamma}^T \boldsymbol{\Upsilon}^T \frac{\partial \boldsymbol{M}}{\partial \gamma} \right\rangle_o \quad . \end{aligned} \tag{3.46}$$

Here, the first and third terms yield to zero upon choosing $\eta = \frac{\partial \omega_i}{\partial \gamma}$ in (3.32a). For the remaining terms, derivative of $\boldsymbol{M}$ is expanded as $\frac{\partial \boldsymbol{M}}{\partial \gamma} = -\boldsymbol{M} \frac{\partial \boldsymbol{P}}{\partial \gamma} \boldsymbol{M}$, and for a more compact notation $\boldsymbol{E} = \frac{\partial \boldsymbol{P}}{\partial \gamma} \boldsymbol{M}$ is introduced. Therefore the sensitivity of $\boldsymbol{A}$ with respect to γ leads to

$$\begin{aligned}\frac{\partial \boldsymbol{A}}{\partial \gamma} &= -\left\langle a \left(\boldsymbol{\Upsilon} \boldsymbol{M} \frac{\partial \boldsymbol{P}}{\partial \gamma} \boldsymbol{M} \boldsymbol{\Gamma}^{T} \; + \boldsymbol{\Gamma} \boldsymbol{M} \frac{\partial \boldsymbol{P}}{\partial \gamma} \boldsymbol{M} \boldsymbol{\Upsilon}^{T} \right) \right\rangle \\ &= -\left\langle a \left(\boldsymbol{\lambda} \frac{\partial \boldsymbol{P}}{\partial \gamma} \boldsymbol{M} \boldsymbol{\Gamma}^{T} \; + \boldsymbol{\Gamma} \boldsymbol{M} \frac{\partial \boldsymbol{P}}{\partial \gamma} \boldsymbol{\lambda}^{T} \right) \right\rangle \\ &= -\left\langle a \left(\boldsymbol{\lambda} \, \boldsymbol{E} \, \boldsymbol{\Gamma}^{T} \; + \boldsymbol{\Gamma} \, \boldsymbol{E}^{T} \, \boldsymbol{\lambda}^{T} \right) \right\rangle \quad .\end{aligned} \tag{3.47}$$

For $\boldsymbol{C}$, the derivative is taken using the form in (3.35)

$$\begin{aligned}\frac{\partial \boldsymbol{C}}{\partial \gamma} &= \frac{\partial}{\partial \gamma} \left\langle \boldsymbol{\Gamma} \boldsymbol{\Phi}^{T} \right\rangle \\ &= \left\langle \frac{\partial \boldsymbol{\lambda}}{\partial \gamma} \, \boldsymbol{\Phi}^{T} \right\rangle_{o} + \; \left\langle \boldsymbol{\Gamma} \, a \, \frac{\partial \boldsymbol{\Lambda}^{T}}{\partial \gamma} \right\rangle_{o} ,\end{aligned} \tag{3.48}$$

and the relevant corrector field gradient is decomposed as

$$\begin{aligned}\boldsymbol{\Theta} &= \nabla_{o} \boldsymbol{\Omega} \\ \boldsymbol{\Lambda} &= \boldsymbol{\Theta} \boldsymbol{M} \quad .\end{aligned} \tag{3.49}$$

Using this decomposition and (3.45), (3.48) takes the form

$$\begin{aligned}\frac{\partial \boldsymbol{C}}{\partial \gamma} &= \left\langle \frac{\partial (\boldsymbol{\Upsilon} \boldsymbol{M})}{\partial \gamma} \, \boldsymbol{\Phi}^{T} \right\rangle_{o} + \left\langle \boldsymbol{\Gamma} \, a \, \frac{\partial (\boldsymbol{\Theta} \boldsymbol{M})^{T}}{\partial \gamma} \right\rangle_{o} \\ &= \left\langle \frac{\partial \boldsymbol{\Upsilon}}{\partial \gamma} \boldsymbol{M} \boldsymbol{\Phi}^{T} \right\rangle_{o} + \left\langle \boldsymbol{\Upsilon} \frac{\partial \boldsymbol{M}}{\partial \gamma} \boldsymbol{\Phi}^{\mathbf{T}} \right\rangle_{o} + \left\langle \boldsymbol{\Gamma} a \boldsymbol{M}^{T} \frac{\partial \boldsymbol{\Theta}^{T}}{\partial \gamma} \right\rangle_{o} + \left\langle \boldsymbol{\Gamma} a \frac{\partial \boldsymbol{M}^{T}}{\partial \gamma} \boldsymbol{\Theta}^{T} \right\rangle_{o} .\end{aligned} \tag{3.50}$$

Here, the first averaging integral is eliminated by choosing $\frac{\partial \lambda_i}{\partial \gamma}$ for η in (3.32a) and third integral is eliminated by choosing $\frac{\partial \Omega_i}{\partial \gamma}$ for θ in (3.32b). For the remaining terms, derivative of $\boldsymbol{M}$ is expanded, which makes the final form for the sensitivity of $\boldsymbol{C}$ with respect to γ as follows

$$\begin{aligned}\frac{\partial \boldsymbol{C}}{\partial \gamma} &= = -\left\langle \boldsymbol{\Upsilon} \boldsymbol{M} \frac{\partial \boldsymbol{P}}{\partial \gamma} \boldsymbol{M} \boldsymbol{\Phi}^{\mathbf{T}} \right\rangle_{o} + \left\langle \boldsymbol{\Gamma} a \boldsymbol{M}^{T} \frac{\partial \boldsymbol{P}^{T}}{\partial \gamma} \boldsymbol{M}^{T} \boldsymbol{\Theta}^{T} \right\rangle_{o} \\ &= -\left\langle \boldsymbol{\lambda} \frac{\partial \boldsymbol{P}}{\partial \gamma} \boldsymbol{M} \boldsymbol{\Phi}^{T} \right\rangle_{o} + \left\langle \boldsymbol{\Gamma} a \boldsymbol{M}^{T} \frac{\partial \boldsymbol{P}^{T}}{\partial \gamma} \boldsymbol{\Lambda}^{T} \right\rangle_{o} \\ &= -\left\langle \boldsymbol{\lambda} \, \boldsymbol{E} \, \boldsymbol{\Phi}^{T} + \; a \, \boldsymbol{\Gamma} \, \boldsymbol{E}^{T} \, \boldsymbol{\Lambda}^{T} \right\rangle \quad .\end{aligned} \tag{3.51}$$

On the other hand, for $\boldsymbol{F}$, first an alternative form is obtained by subtracting the transpose of (3.32b) from (3.36) where $\theta = \Omega_i$

$$\begin{aligned} \boldsymbol{F} &= \left\langle e\boldsymbol{I} - b\boldsymbol{\Lambda}^T \right\rangle - \left\langle (\boldsymbol{\Phi}\boldsymbol{\nabla}_{\boldsymbol{y}}\boldsymbol{\Omega})^T \right\rangle \\ &= \left\langle e\boldsymbol{I} - b\boldsymbol{\Lambda}^T \right\rangle - \left\langle \boldsymbol{\Lambda}(b\boldsymbol{I} + a\boldsymbol{\Lambda}^T) \right\rangle \\ &= \left\langle e\boldsymbol{I} - b(\boldsymbol{\Lambda} + \boldsymbol{\Lambda}^T) - a\boldsymbol{\Lambda}\boldsymbol{\Lambda}^T \right\rangle \quad . \end{aligned} \tag{3.52}$$

The direct derivative of $\boldsymbol{F}$ delivers

$$\begin{aligned} \frac{\partial \boldsymbol{F}}{\partial \gamma} &= -\left\langle b\,\frac{\partial \boldsymbol{\Lambda}}{\partial \gamma} \right\rangle_o - \left\langle b\,\frac{\partial \boldsymbol{\Lambda}^T}{\partial \gamma} \right\rangle_o - \left\langle a\,\frac{\partial \boldsymbol{\Lambda}}{\partial \gamma}\,\boldsymbol{\Lambda}^T \right\rangle_o - \left\langle a\,\boldsymbol{\Lambda}\,\frac{\partial \boldsymbol{\Lambda}^T}{\partial \gamma} \right\rangle_o \\ &= -\left\langle \frac{\partial \boldsymbol{\Lambda}}{\partial \gamma}(b\boldsymbol{I} + a\boldsymbol{\Lambda}^T) \right\rangle_o - \left\langle (b\boldsymbol{I} + a\boldsymbol{\Lambda})\frac{\partial \boldsymbol{\Lambda}^T}{\partial \gamma} \right\rangle_o \\ &= -\left\langle \frac{\partial \boldsymbol{\Lambda}}{\partial \gamma}\,\boldsymbol{\Phi}^T \right\rangle_o - \left\langle \boldsymbol{\Phi}\,\frac{\partial \boldsymbol{\Lambda}^T}{\partial \gamma} \right\rangle_o , \end{aligned} \tag{3.53}$$

which, through the substitution of $\boldsymbol{M}$, leads to

$$\begin{aligned} \frac{\partial \boldsymbol{F}}{\partial \gamma} &= -\left\langle \frac{\partial(\boldsymbol{\Theta}\boldsymbol{M})}{\partial \gamma}\boldsymbol{\Phi}^T \right\rangle_o - \left\langle \boldsymbol{\Phi}\frac{\partial(\boldsymbol{\Theta}\boldsymbol{M})^T}{\partial \gamma} \right\rangle_o \\ &= -\left\langle \boldsymbol{\Theta}\frac{\partial \boldsymbol{M}}{\partial \gamma}\boldsymbol{\Phi}^T \right\rangle_o - \left\langle \frac{\partial \boldsymbol{\Theta}}{\partial \gamma}\boldsymbol{M}\boldsymbol{\Phi}^T \right\rangle_o - \left\langle \boldsymbol{\Phi}\frac{\partial \boldsymbol{M}^T}{\partial \gamma}\boldsymbol{\Theta}^T \right\rangle_o - \left\langle \boldsymbol{\Phi}\boldsymbol{M}^T\frac{\partial \boldsymbol{\Theta}^T}{\partial \gamma} \right\rangle_o \quad . \end{aligned} \tag{3.54}$$

The second and fourth term vanish upon choosing $\theta = \frac{\partial \Omega_i}{\partial \gamma}$ at (3.32b). For the remaining terms, sensitivity of $\boldsymbol{F}$ with respect to γ takes the final form by applying the expansion with $\boldsymbol{M}$

$$\begin{aligned} \frac{\partial \boldsymbol{F}}{\partial \gamma} &= \left\langle \boldsymbol{\Theta}\boldsymbol{M}\frac{\partial \boldsymbol{P}}{\partial \gamma}\boldsymbol{M}\boldsymbol{\Phi}^T \right\rangle + \left\langle \boldsymbol{\Phi}\boldsymbol{M}^T\frac{\partial \boldsymbol{P}^T}{\partial \gamma}\boldsymbol{M}^T\boldsymbol{\Theta}^T \right\rangle \\ &= \left\langle \boldsymbol{\Lambda}\boldsymbol{E}\boldsymbol{\Phi}^T \right\rangle + \left\langle \boldsymbol{\Phi}\boldsymbol{E}^T\boldsymbol{\Lambda}^T \right\rangle \quad . \end{aligned} \tag{3.55}$$

Chapter 4

Finite Element Analysis

In this chapter, the finite element (FE) formulation for the cell problems and the discritization scheme is introduced. The overall optimization framework employs an in-house FE code as its kernel on which cell problems, homogenized coefficients and their derivatives are calculated.

4.1 Cell Problems in Weak Form

In order to calculate the homogenized coefficients, cell problems are solved via FE method. In this section the derivation of the weak form of the cell problems are presented. First, invoking the summation convention, the cell problems (3.13) are expressed as

$$\frac{\partial}{\partial y_i}(a\frac{\partial \omega_j}{\partial y_i}) = -\frac{\partial a}{\partial y_j} \tag{4.1a}$$

$$\frac{\partial}{\partial y_i}(a\frac{\partial \Omega_j}{\partial y_i}) = -\frac{\partial b}{\partial y_j}. \tag{4.1b}$$

A more compact notation may be adopted as follows:

$$(a\,\omega_{j,i})_{,i} = -a_{,j} \tag{4.2a}$$

$$(a\,\Omega_{j,i})_{,i} = -b_{,j}. \tag{4.2b}$$

For the weak forms, (4.2a) is discussed first by introducing the residual

$$r = (a\,\omega_{j,i})_{,i} + a_{,j} = 0. \tag{4.3}$$

The residual is then multiplied by a test function η and integrated over the unit domain. Note that notations Ω and Γ will be used for domain and boundary integrals respectively:

$$\int_\Omega \eta r\, d\Omega = \int_\Omega \eta(a\,\omega_{j,i})_{,\,i} + a_{,\,j}\, d\Omega = 0. \tag{4.4}$$

Applying the chain rule, one obtains

$$\int_\Omega (\eta a\omega_{j,i})_{,\,i}\, d\Omega - \int_\Omega \eta_{,i} a\omega_{j,i}\, d\Omega + \int_\Omega (\eta a)_{,\,j}\, d\Omega - \int_\Omega \eta_{,\,j}\, a\, d\Omega = 0. \tag{4.5}$$

The first and the third integrals are converted into boundary integrals using the divergence theorem:

$$\int_\Gamma \eta a\,\omega_{j,\,i}\, n_i\, d\Gamma - \int_\Omega \eta_{,i}\, a\omega_{j,i}\, d\Omega + \int_\Gamma \eta a\, n_j\, d\Gamma - \int_\Omega \eta_{,\,j}\, a\, d\Omega = 0. \tag{4.6}$$

The boundary integrals are typically decomposed into Dirichlet and Neumann boundary conditions for the most general scenario. However, in the present setting, boundary conditions are of mixed type, namely periodic, which immediately eliminates both integrals. This can be observed by investigating individual terms in the boundary integrals. Both η and $\boldsymbol{\omega}$ are periodic whereas normal vector $\boldsymbol{n}$ anti-periodic. Therefore these integrals vanish. Accordingly, the weak form of the first cell problem delivers

$$\int_\Omega \eta_{,i}\, a\omega_{j,i}\, d\Omega = -\int_\Omega \eta_{,\,j} a\, d\Omega. \tag{4.7}$$

Following the same procedure, weak form for the second set of cell problems are obtained as

$$\int_\Omega \eta_{,i} a\Omega_{j,i}\, d\Omega = -\int_\Omega \eta_{,j}\, b\, d\Omega. \tag{4.8}$$

4.2 Finite Element Discretization

In order to build the linear system of equations, 2D domain is discretized into $N_e = N_x \times N_y$ elements with N_n noded shape functions for the unknown fields and test function η. Since the procedure is same for both set of the cell problems, derivation of the first one is discussed and the result is given for both sets. Discritization for the unknown vector fields ω_j and test function η is

$$\eta_e = \sum_{I}^{N_n} \eta_e^I N^I(\xi) \tag{4.9a}$$

$$(\omega_j)_e = \sum_{J}^{N_n} (\omega_j)_e^J N^J(\xi) \tag{4.9b}$$

where I, J represent node indices, j represents the index for each cell problem for the first set of cell problems and e represents elements. Shape functions are demonstrated with N^I for the master element with the coordinates $\boldsymbol{\xi}$. Plugging these in the weak form, one obtains

$$\sum_{e}^{N_e}\sum_{I}^{N_n}\eta_e^I\sum_{J}^{N_n}\left(\int_\Omega N_{,i}^I a_e N_{,i}^J d\Omega\right)(\omega_j)_e^J = -\sum_{e}^{N_e}\sum_{I}^{N_n}\eta_e^I\left(\int_\Omega N_{,j}^I a_e \, d\Omega\right). \tag{4.10}$$

Since shape functions live on the master element, derivatives should also be adjusted accordingly. For this purpose, isoparametric mapping is introduced

$$(y_i)_e = \sum_{I=1}^{N_n} (y_i)_e^I N^I. \tag{4.11}$$

Subsequently, the derivatives are expanded as

$$\frac{\partial(.)}{\partial y_i} = \frac{\partial(.)}{\partial \xi_k}\frac{\partial \xi_k}{\partial y_i}. \tag{4.12}$$

The gradient of mapping from reference configuration to master element is indicated as $\boldsymbol{F}$ and calculated for each element via

$$\frac{\partial y_i}{\partial \xi_k} = F_{ik} = \sum_{I=1}^{N_n} y_i^I \frac{\partial N^I}{\partial \xi_k}. \tag{4.13}$$

Also, the integral domain is mapped as

$$d\Omega = J d\Omega^\square \tag{4.14}$$

where $J = det(\boldsymbol{F})$ and $\Omega^\square$ is the domain of the master element. Using these adjustments and eliminating η_e^I from both sides, (4.10) takes the form

$$\begin{aligned}\sum_{I}^{N_n}\sum_{J}^{N_n}\left(\int_{\Omega^\square}\bar{F}_{ik}\frac{\partial N^I(\boldsymbol{\xi})}{\partial \xi_k}\cdot a\bar{F}_{ik}\frac{\partial N^J(\boldsymbol{\xi})}{\partial \xi_k}Jd\Omega^\square\right)(\omega_j)_e^J = \\ -\sum_{I}^{N_n}\left(\int_{\Omega^\square}\bar{F}_{jk}\frac{\partial N^I(\boldsymbol{\xi})}{\partial \xi_k}a\,Jd\Omega^\square\right)\end{aligned} \tag{4.15}$$

where the inverse of gradient mapping $\boldsymbol{F}$ is denoted with $\bar{\boldsymbol{F}}$. In this format, all derivatives can be calculated since they are taken with respect to $\boldsymbol{\xi}$. Note that only the derivatives of shape functions are used for FE discretization. For a compact notation of all the terms together, node dependent quantities inside the integrals are grouped as

$$\bar{F}_{ik}\frac{\partial N^I(\boldsymbol{\xi})}{\partial \xi_k} \cdot \bar{F}_{ik}\frac{\partial N^J(\boldsymbol{\xi})}{\partial \xi_k} = k^{IJ}(\xi) \tag{4.16a}$$

$$\bar{F}_{jk}\frac{\partial N^I(\boldsymbol{\xi})}{\partial \xi_k} = b^I_j(\xi). \tag{4.16b}$$

Note that the sum over the nodes are explicitly demonstrated. Also, the calculations for $k^{IJ}(\xi)$ and $b^I_j(\xi)$ are conducted elementwise; however this is not shown explicitly with an index.

Finally, for the calculation of integrals, numerical integration is performed using Gaussian quadrature. For the 2D problem, numerical quadrature for a function $f = f(\boldsymbol{\xi})$ follows

$$\int_{\Omega^\square} w_{g_i} f(\boldsymbol{\xi})\Omega^\square = \sum_{g_1}^{N_g}\sum_{g_2}^{N_g} w_{g_1}w_{g_2} f(\boldsymbol{\xi}(g_1, g_2)) \tag{4.17}$$

where g_i represent the quadrature points and w_{g_i} represent the quadrature weights. Afterwards, these quantities are substituted in (4.15)

$$\sum_{e}^{N} a_e \sum_{I}^{N_n}\sum_{J}^{N_n}\left(\sum_{g_1}^{N_g}\sum_{g_2}^{N_g} w_{g_1}w_{g_2}\, k^{IJ}\right)(\omega_j)^J_e = -\sum_{e}^{N} a_e \sum_{I}^{N_n}\left(\sum_{g_1}^{N_g}\sum_{g_2}^{N_g} w_{g_1}w_{g_2}\, b^I_j\right) \tag{4.18}$$

where element matrix components are

$$(K^{IJ})^e = a_e \sum_{g_1}^{N_g}\sum_{g_2}^{N_g} w_{g_1}w_{g_2}\, k^{IJ}, \tag{4.19}$$

and right hand side vector is

$$(B^I_j)^e = a_e \sum_{g_1}^{N_g}\sum_{g_2}^{N_g} w_{g_1}w_{g_2}\, b^I_j. \tag{4.20}$$

Note that variables a, b and e are assumed to be constants over an element in view of the upcoming optimization formulation. For the second set of cell problems, element matrix is same as the first set. However, for the right hand side vector, coefficient changes which is named as

$$(D^I_j)^e = b_e \sum_{g_1}^{N_g} \sum_{g_2}^{N_g} w_{g_1} w_{g_2} \, b^I_j. \tag{4.21}$$

Therefore the cell problems take the form of a system of four equations

$$\sum_{e}^{N_e} \sum_{J}^{N_n} (K^{IJ})^e (\omega_1)^J_e = -\sum_{e}^{N_e} (B^I_1)^e \tag{4.22a}$$

$$\sum_{e}^{N_e} \sum_{J}^{N_n} (K^{IJ})^e (\omega_2)^J_e = -\sum_{e}^{N_e} (B^I_2)^e \tag{4.22b}$$

$$\sum_{e}^{N_e} \sum_{J}^{N_n} (K^{IJ})^e (\Omega_1)^J_e = -\sum_{e}^{N_e} (D^I_1)^e \tag{4.22c}$$

$$\sum_{e}^{N_e} \sum_{J}^{N_n} (K^{IJ})^e (\Omega_2)^J_e = -\sum_{e}^{N_e} (D^I_2)^e. \tag{4.22d}$$

Note that the summation over the elements indicate the assembly operation. In this work, $N_x = N_y = 40$ is chosen for the disretization with $N_n = 4$ noded linear quadrilateral elements. For the solution of homogenization problems, typically one of the three boundary conditions is implemented which are linear displacement, periodic or traction boundary condition. Here, equations in (4.22) are solved using periodic boundary conditions for the reciprocal surfaces. Uniqueness is imposed by assigning homogeneous Dirichlet boundary conditions for a corner node.

4.3 Flow and Stress Factor Tensors

After the unknown vector fields $\boldsymbol{\omega}$ and $\boldsymbol{\Omega}$ are found, they are used to calculate the homogenized coefficients and their sensitivities. In this section implementation for numerical averaging is given for the homogenized coefficients. For the calculation of each tensor, any of the alternative expression that are introduced so far can be used. Here, definitions that are used in the code implementation are introduced.

Starting with $\boldsymbol{A}$, the definition in (3.34) is implemented via

$$\boldsymbol{A} = \langle \Gamma_k^i a \Gamma_k^j \rangle = \int_\Omega \left((\delta_{ik} + \frac{\partial \omega_i}{\partial y_k}) a (\delta_{jk} + \frac{\partial \omega_j}{\partial y_k}) \right) d\Omega \tag{4.23}$$

where the division by the domain area is not explicitly shown since the unit domain is employed. For the numerical integration, vector fields are discritized as in (4.9b)

$$\boldsymbol{A} = \int_\Omega \left(\left(\delta_{ik} + \frac{\partial \left(\sum_I \omega_i^I N^I \right)}{\partial y_k} \right) a \left(\delta_{jk} + \frac{\partial \left(\sum_J \omega_j^J N^J \right)}{\partial y_k} \right) \right) d\Omega. \tag{4.24}$$

Accordingly, derivatives are adjusted based on (4.12):

$$\boldsymbol{A} = \int_\Omega \left(\left(\delta_{ik} + \sum_I \omega_i^I \bar{F}_{mk} \frac{\partial N^I}{\partial \xi_m} \right) a \left(\delta_{jk} + \sum_J \omega_j^J \bar{F}_{nk} \frac{\partial N^J}{\partial \xi_n} \right) \right) d\Omega. \tag{4.25}$$

For the geometry optimization, the change in the unit cell shape was allowed, during which the area of the unit cell also changes. In order to account for these changes, $\boldsymbol{F}$ is not calculated with respect to the reference domain but to current domain which changes with $\boldsymbol{P}$, the linear mapping introduced in Chapter 2. The alterations in the area are resolved by dividing the integration by $det(\boldsymbol{P})$ because the area of the current domain is equal to $det(\boldsymbol{P})$ multiplied by the area of the reference unit domain. Subsequently, the integration domain is changed from current to master domain via $d\Omega = J d\Omega^\square$ and integral is performed via Gaussian quadrature

$$A_{ij} = \frac{1}{det(\boldsymbol{P})} \sum_{gp_1} \sum_{gp_2} \left(\left(\delta_{ik} + \sum_I \omega_i^I \bar{F}_{mk} \frac{\partial N^I}{\partial \xi_m} \right) a \left(\delta_{jk} + \sum_J \omega_j^J \bar{F}_{mk} \frac{\partial N^J}{\partial \xi_m} \right) \right) J w_1 w_2 \tag{4.26}$$

where w_1 and w_2 are Gaussian weights. A similar numerical integration is followed for $\boldsymbol{C}$ in (3.35) and $\boldsymbol{F}$ in (3.52) where final form delivers

$$C_{ij} = \frac{1}{det(\boldsymbol{P})} \sum_{gp_1} \sum_{gp_2} \left(\left(\delta_{ik} + \sum_I \omega_i^I \bar{F}_{mk} \frac{\partial N^I}{\partial \xi_m} \right) \left(b\delta_{jk} + a \sum_J \Omega_j^J \bar{F}_{mk} \frac{\partial N^J}{\partial \xi_m} \right) \right) J w_1 w_2 \tag{4.27}$$

$$\begin{aligned} F_{ij} = \frac{1}{det(\boldsymbol{P})} \sum_{gp_1} \sum_{gp_2} \Bigg(& e\delta_{ik} - b \left(\sum_I \Omega_i^I \bar{F}_{mj} \frac{\partial N^I}{\partial \xi_m} + \sum_J \Omega_j^J \bar{F}_{mi} \frac{\partial N^J}{\partial \xi_m} \right) \\ & - \left(\sum_K \Omega_i^K \bar{F}_{mk} \frac{\partial N^K}{\partial \xi_m} \right) \Bigg) J w_1 w_2 \end{aligned} \tag{4.28}$$

For the sensitivities, a similar format follows.

Chapter 5

Optimization Problems

In this chapter, optimization scheme is described in detail. This scheme allows different objective functions and constraints to be used in varied combinations. The introduced scheme consists of three options which are space, time and geometry optimizations.

5.1 Design Variables

For optimization, design variables are updated at each iteration using sensitivity based optimization algorithm MMA [41]. These design variables are grouped under film thickness design variables which are associated with spatial and temporal variations and geometry design variables which control the shape of the unit cell. All design variables are set between 0 and 1, and for film thickness design variables filtering is employed.

5.1.1 Film Thickness Design Variables

In order to obtain suitable surface textures for the targeted response, film thickness is controlled via solid isotropic material with penalization (SIMP) method [54]. Film thickness is described using spatial and the temporal design variables. Spatial design variables determine the distribution of the film thickness over the domain at any given time instance. On the other hand, temporal design variables control the active motion for each time step. Hence, both spatial and temporal variables are referred to as film thickness design variables.

In the optimization scheme, spatial design variables are denoted with s_i and represented via element-wise shape functions $\hat{N}$ which are 1 within an element and 0 elsewhere:

$$\boldsymbol{s} = \sum_{I}^{N_e} \hat{N}^I s^I. \tag{5.1}$$

Note that boldface notation for optimization variables refer to their distribution. The distribution of the spatial design variables is shown in Figure 5.1.

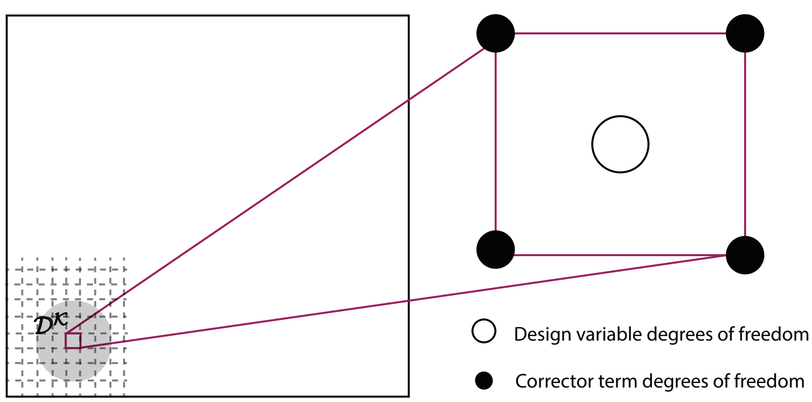

Figure 5.1: *The unit cell and the elementwise design variables are depicted along with the filtering domain $\mathcal{D}^K$*

During optimization, this distribution is filtered in order to avoid checkerboard patterns and other mesh-dependent problems [55]. Several different filters and radii were studied by Waseem et al. where it has been observed that linear density filter can allow smooth transitions on the film thickness variation [56]. Smooth variation is associated with 0-to-1 textures where the transitions from peaks to valleys are soft contrary to 0-or-1 designs where these transitions are sharp. The latter outcome is preferred for this work since texture is expected to have a gradually varying surface. The filtered $\boldsymbol{s}$ is denoted with $\boldsymbol{\rho}$ and obtained via

$$\boldsymbol{\rho} = \sum_{K}^{N_e} \hat{N}^K \rho^K = \sum_{K}^{N_e} \hat{N}^K \mathcal{F}(\mathcal{D}^K, s). \tag{5.2}$$

For the filtering, a conic weight is used that covers a domain $\mathcal{D}$, which is also demonstrated in Figure 5.1. It is previously indicated that setting the radius of the filter to approximately $N_x/10$ is a good choice [56], therefore in the present setting radius of 4 is employed. The conic weights of the filter are defined as

$$w^{KI} = \begin{cases} \frac{R-d(K,I)}{\sum_{J\in\mathcal{D}^J} R-d(K,J)} & I \in \mathcal{D}^K \\ 0 & \text{otherwise} \end{cases} \tag{5.3}$$

where $\sum_I w^{KI} = 1$ [57, 58]. By using the conic weights, linear density filter and its sensitivity takes the following form:

$$\begin{aligned} &Filter: \; \rho^K = \mathcal{F}(\mathcal{D}^K, s) = \sum_I w^{KI} s^I, \\ &Sensitivity: \; \frac{\partial \rho^K}{\partial s^I} = w^{KI}. \end{aligned} \tag{5.4}$$

For the surface characterization, minimum and maximum values for film thickness is set as H_{min} and H_{max} as illustrated in Figure 5.2 and the interpolation takes the premature form of

$$h(\boldsymbol{y}) = H_{min} + (H_{max} - H_{max})\rho(\boldsymbol{y})^{\eta}. \tag{5.5}$$

Here, h describes the film thickness distribution among the unit cell. The exponent η is used for creating surfaces with different transitional areas. For $\eta > 1$ transition from valley to peak points are sharp whereas for $\eta = 1$ a linear transition is obtained. Similar to filter preferences, here also $\eta = 1$ will be chosen for a more smooth surface description and it is not shown explicitly for further discussion.

During the time-dependent change, the surface average h_0 of a micro-texture should be kept constant. For this purpose, an alternative for the interpolation (5.5) is derived. First, a positive deviation $\bar{h}^+$ and negative deviation $\bar{h}^-$ is calculated as depicted in Figure 5.2:

$$\begin{aligned} \bar{h}^+ &= H_{max} - h_0 \\ \bar{h}^- &= H_{min} - h_0 \end{aligned} \tag{5.6}$$

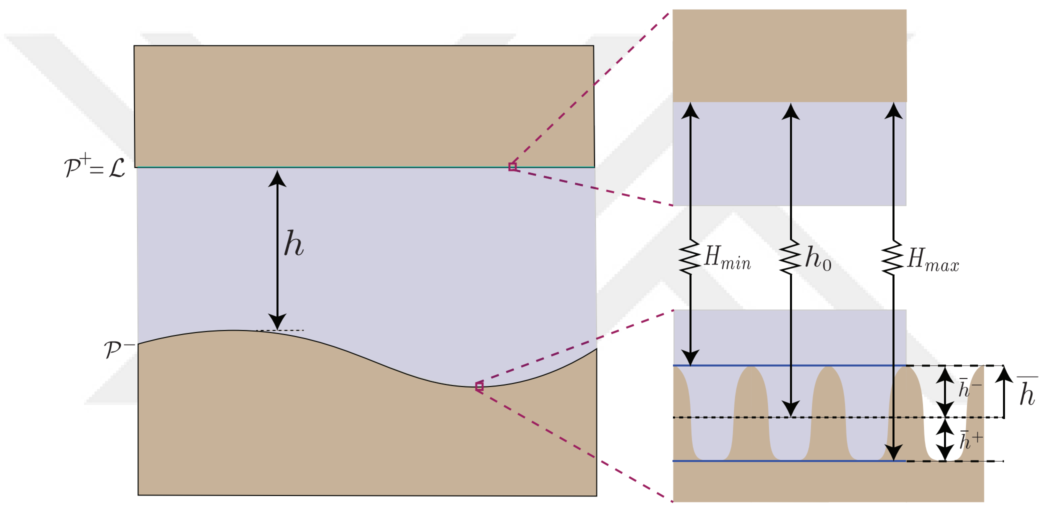

Figure 5.2: *Demonstration of the variables implemented in the interpolation functions for the unilateral lubrication setting*

Using these changes, (5.5) is rewritten as:

$$h(y) = h_0 + \bar{h}(\boldsymbol{y}) \tag{5.7a}$$

$$\bar{h}(\boldsymbol{y}) = h^- + (h^+ - h^-)\rho(\boldsymbol{y}) \tag{5.7b}$$

For time optimization, a period is discritized into N_t time steps which is an arbitrary number and set to $N_t = 18$ for the present work. The temporal design variable $\boldsymbol{k}(t)$ is introduced which controls change of the surface texture at each time step. Similar to spatial design variables, temporal design variables are discretized with shape functions $\tilde{N}$ which are 1 at a given time step and 0 everywhere else:

$$\boldsymbol{k} = \sum_{L}^{N_t} \tilde{N}^L k^L. \tag{5.8}$$

However, $\boldsymbol{k}$ controls each time step independently, which may create jumps in the consequent time steps unlike a realizable signal. To overcome such a problem, time filtering is imposed to $\boldsymbol{k}$ and $\boldsymbol{\tau}(t)$ is obtained via linear filter, $\boldsymbol{\tau} = \mathcal{F}(\mathcal{D}, k)$. Here, time filtering has the same procedure as the space filtering, however the domain $\mathcal{D}^M$ states a time interval instead of an area, and a single time step is chosen as the radius of the filter. Note that both space and time filters are employed periodically.

In order to introduce τ to calculations, it is also discretized via element-wise shape functions for each time step t

$$\boldsymbol{\tau} = \sum_{M}^{N_t} \tilde{N}^K \tau^M = \sum_{M}^{N_t} \tilde{N}^K \mathcal{F}(\mathcal{D}^M, k). \tag{5.9}$$

To integrate this temporal change, interpolation in (5.7a) is rewritten with the addition of τ

$$h(\boldsymbol{y}, t) = h_0 + \tau(t)\bar{h}(\boldsymbol{y}). \tag{5.10}$$

Using this final form of the interpolation in (5.10), derivatives of the coefficients $a = \frac{h^3}{12\mu}, b = \frac{h}{2}$ and $e = \frac{\mu}{h}$ are evaluated with respect to s for each element,

$$\frac{\delta a}{\delta s} = \frac{\delta(\frac{h^3}{12\mu})}{\delta h} \frac{\delta h}{\delta \rho} \frac{\delta \rho}{\delta s} \tag{5.11a}$$

$$\frac{\delta b}{\delta s} = \frac{\delta(\frac{h}{2})}{\delta h} \frac{\delta h}{\delta \rho} \frac{\delta \rho}{\delta s} \tag{5.11b}$$

$$\frac{\delta e}{\delta s} = \frac{\delta(\frac{\mu}{h})}{\delta h} \frac{\delta h}{\delta \rho} \frac{\delta \rho}{\delta s} \tag{5.11c}$$

and with respect to k for each time step

$$\frac{\delta a}{\delta k} = \frac{\delta(\frac{h^3}{12\mu})}{\delta h} \frac{\delta h}{\delta \tau} \frac{\delta \tau}{\delta k} \tag{5.12a}$$

$$\frac{\delta b}{\delta k} = \frac{\delta(\frac{h}{2})}{\delta h} \frac{\delta h}{\delta \tau} \frac{\delta \tau}{\delta k} \tag{5.12b}$$

$$\frac{\delta e}{\delta k} = \frac{\delta(\frac{\mu}{h})}{\delta h} \frac{\delta h}{\delta \tau} \frac{\delta \tau}{\delta k} \tag{5.12c}$$

where the derivative of the interpolation (5.7) with respect to filtered design variables delivers

$$\frac{\delta h}{\delta \rho} = \tau(h^+ - h^-) \tag{5.13a}$$

$$\frac{\delta h}{\delta \tau} = \bar{h}. \tag{5.13b}$$

Note that the variable shown with ζ in subsection 3.2.1 can refer either to s or k in this arrangement.

5.1.2 Geometry Design Variables

Geometry design variables control the shape of the unit cell by controlling the components of linear transformation tensor $\boldsymbol{P}$, which will be controlled through design variables γ_i following the notation used in section 3.2.2. In order to limit the minimum and maximum values of each index in $\boldsymbol{P}$, the components are now expressed as

$$[P] = \begin{bmatrix} g_{max}\gamma_1 + g_{min}(1-\gamma_1) & 2d(\gamma_2 - 0.5) \\ 2d(\gamma_3 - 0.5) & g_{max}\gamma_4 + g_{min}(1-\gamma_4) \end{bmatrix}$$

where g_{max}, g_{min} and d are the scaling constants for controlling the transformation amount of the unit cell. These scaling constants are implemented for the practicality of using each index within a designated interval because γ moves between $(0,1)$. In other words, P_{11} and P_{22} can take a value between g_{max} and g_{min}; wheras the diagonal components move between $(-d,d)$. Thereby, sensitivities of $\boldsymbol{P}$ with respect to γ are written directly in terms of these scaling constants.

5.2 Objective Functions

In the optimization scheme, a target flux or traction signal is prescribed and the aim is to capture these signals by adjusting the design variables. Therefore objective function is written as an aggregate error between calculated and the current flux or traction. Target response is demonstrated with $\boldsymbol{Q}^*$ for flux and with $\mathcal{T}^*$ for traction so that objective functions takes the form

$$\boldsymbol{\sigma}^{\boldsymbol{Q}} = \left(\frac{1}{T} \int_{t-T}^{t} \sum_i \left(\frac{Q_i(t) - Q_i^*(t)}{Q_i^*(t)} \right)^2 \mathrm{d}t \right)^{\frac{1}{2}} \tag{5.14a}$$

$$\boldsymbol{\sigma}^{\mathcal{T}} = \left(\frac{1}{T} \int_{t-T}^{t} \sum_i \left(\frac{\mathcal{T}_i(t) - \mathcal{T}_i^*(t)}{\mathcal{T}_i^*(t)} \right)^2 \mathrm{d}t \right)^{\frac{1}{2}} \tag{5.14b}$$

for flux and traction, respectively. Here, flux and traction is calculated using (3.23) and (3.30).

In the objective functions, denominators are included to normalize the difference; so that objective can cover the changes on Q_1 and Q_2 that have different peak-to-peak amplitudes. However, when very small values are assigned to $\boldsymbol{Q}^*$ or $\mathcal{T}^*$ as targets, denominators cause numerical problems. Therefore if the values of $Q_i^*(t)$ and $\mathcal{T}_i^*(t)$ are smaller than 0.01, denominators are replaced with 0.01.

Within the optimization scheme, two types of targets are employed which are realizable and unrealizable targets. For the realizable targets, if the objective function can be driven to zero, it will be driven to zero. On the other hand, for the unrealizable targets, perfect objective cannot be obtained but the smallest possible value will be observed if all optimization features (time, space and geometry) are activated. Note that a target may be realizable when all features are activated but might turn into an unrealizable case when one of the features is deactivated.

5.3 Constraints

Depending on the activated optimization scheme, space or geometry constraints are introduced to the system. Space constraint is implemented to keep the avarage of $\bar{h}$ at zero, so that h_0 is preserved. The space constraint is written as

$$\langle \bar{h}(y) \rangle^2 = 0. \tag{5.15}$$

Sensitivity of this constraint is readily found based on (5.7). Additionally, a constraint on the linear transformation tensor is implemented to limit the size of the unit cell during the optimization with

$$(det(\boldsymbol{P}) - 1)^2 = 0. \tag{5.16}$$

The size of the unit cell does not affect the result of homogenization, therefore this constraint is not a necessity but a convenience.

Chapter 6

Numerical Investigations

In this chapter, results from time, space and geometry optimization schemes are presented and compared for target flux and traction signals. Each optimization scheme can work individually or with each other's combination and their contributions are explained one by one since each enhances the design space in a particular way. Within the presented examples flux or traction based objectives are interchangeably employed for the demonstration purposes. Although the proposed system does not require a specific length scale, viscosity μ is taken as 0.14 Pa.s. and μm is assumed for all length scales for completeness. In the following figures, two- and three-dimensional shapes are built using 3×3 unit cells and signals are plotted for three periods.

6.1 Time Optimization

As a first step to optimize a flux or traction signal, time optimization is activated solely. In the examples of this section, target micro-texture is assigned to the framework as an input and only temporal variation is subjected to optimization. In other words, $\bar{h}$ is provided to the optimization scheme whereas the change of temporal design variable τ is initially unknown and found later in optimization.

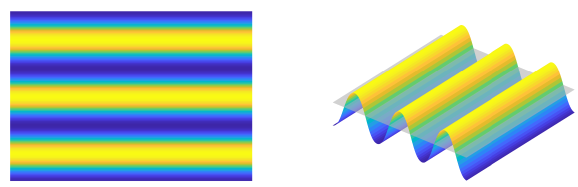

(a) assigned micro-texture ($\bar{h}$)

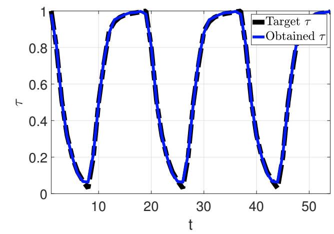

(b) targeted and optimized temporal design variable τ

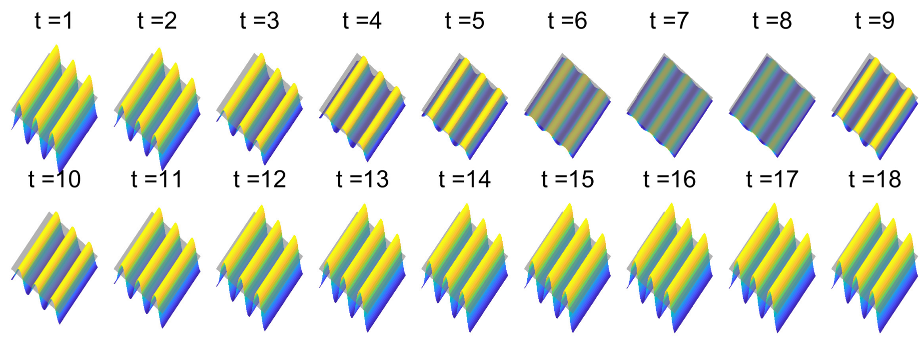

(c) temporal variation of the surface (h) for each time step (t)

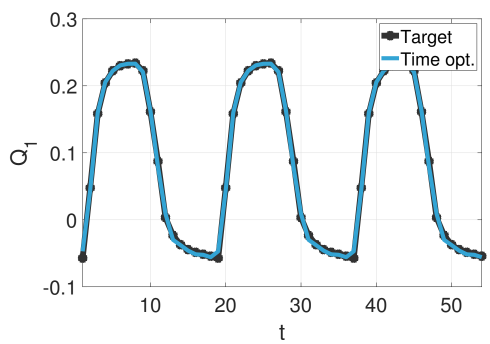

(d) macroscopic flux along x_1

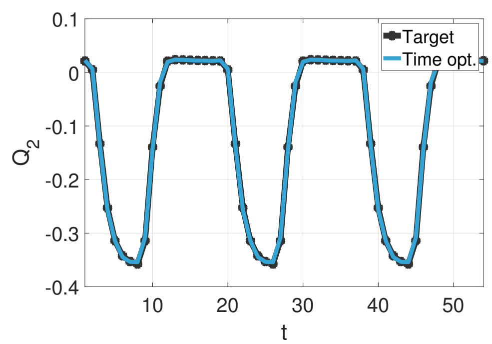

(e) macroscopic flux along x_2

Figure 6.1: *Time optimization for the flux response with the parameters* $H_{max} =$ *1.9,* $H_{min} = 0.1$, $\bar{h}^+ = \bar{h}^- = 0.9$, $h_0 = 1$, $\theta_G = 22.5°$, $\theta_V = 67.5°$ *is illustrated. The assigned micro-texture is chosen as parallel grooves and* τ *is prescribed as a distorted sinusoidal signal.*

For evaluating the objective functions, previously introduced (3.23) is used for flux and (3.30) is used for traction calculations. Target flux ($\boldsymbol{Q}^*$) and traction

($\boldsymbol{\mathcal{T}}^*$) values are found using the homogenized coefficients which are created for an assigned film thickness distribution h for each time step. On the other hand, $\boldsymbol{G}$ and $\boldsymbol{V}$ are chosen in the beginning of an optimization problem and kept constant for both target and prescribed signals throughout the optimization. The magnitudes of $\boldsymbol{G}$ and $\boldsymbol{V}$ are always assigned to unity and only their orientations are changed for different optimization problems. However, they are kept constant throguh time within a given optimization problem although this is not a requirement in the most general setting. From this schematic, the developed algorithm is expected to deliver an optimized flux ($\boldsymbol{Q}$) or traction ($\boldsymbol{\mathcal{T}}$) by adjusting the design parameter τ.

The first example is illustrated in Figure 6.1. Here, τ describes the time variation for the amplitude of a parallel groove micro-texture. The corresponding macroscopic response describes a targeted flux, which is fed into the optimization algorithm. In figure 6.1(a), texture of the active surface is shown in 2D and 3D representations and the time dependent variation of the optimized surface is visualized in figure 6.1(c) for a period, which practically overlaps with the target. This change is controlled by τ which is initially assigned as zero to the framework for all time steps. At the converged optimization, however, target τ, which causes the temporal variation in texture amplitude and therefore in flux, is captured almost one-to-one as shown in figure 6.1(b). The target and the obtained macroscopic flux signals are demonstrated in figure 6.1(d) and figure 6.1(e).

For the second example in Figure 6.2, same procedure is pursued for a macroscopic traction response. In this example, a different micro-texture is prescribed and time variation is similarly subjected to optimization. Again, the target response is perfectly captured.

In both examples, geometry of the unit cell is kept constant, together with the micro-texture topology i.e. $\bar{h}$. Since only the temporal design variable is subjected to optimization, procedure is very efficient and the result is easily acquired by the framework.

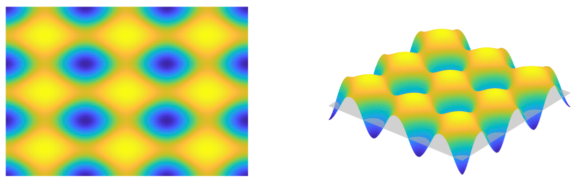

(a) assigned micro-texture ($\bar{h}$)

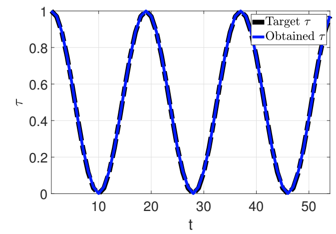

(b) targeted and optimized temporal design variable τ

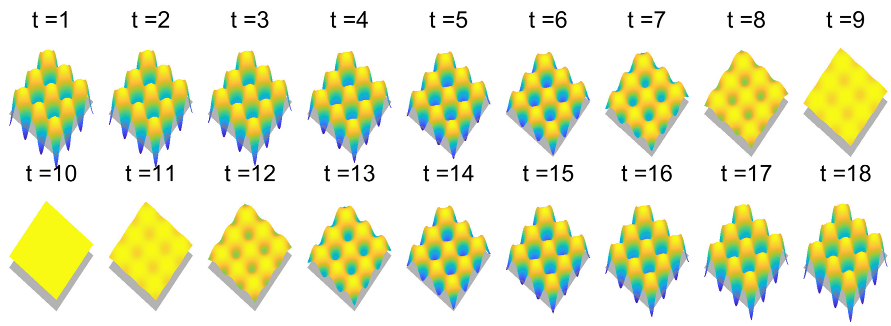

(c) temporal variation of the surface (h) for each time step (t)

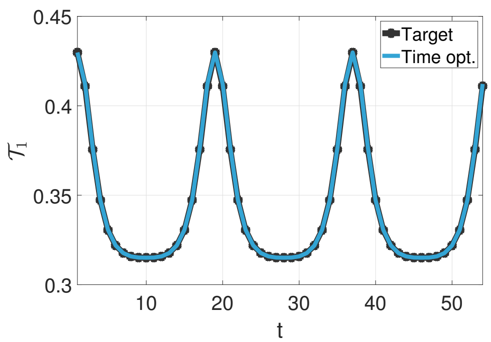

(d) macroscopic traction along x_1

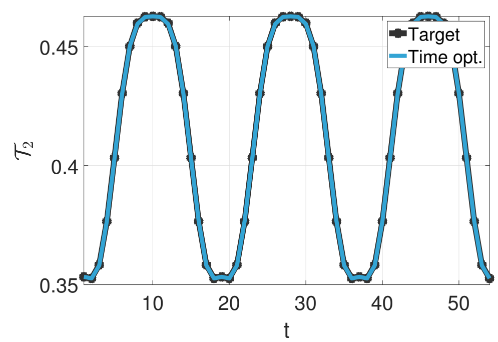

(e) macroscopic traction along x_2

Figure 6.2: *time optimization for the traction response with the parameters* $H_{max} = 2.5$, $H_{min} = 0.1$, $\bar{h}^{+} = \bar{h}^{-} = 0.9$, $h_0 = 0.87$, $\theta_G = 22.5°$, $\theta_V = 67.5°$ *is illustrated. The assigned micro-texture is chosen as sinusoidal hills and temporal change* τ *is prescribed as a sinusoidal signal.*

Note that the variable τ can be associated with an external signal such as electricity, heat or magnetic field that controls the texture and is sensitive to such a physical input. However, presently τ is a non-physical design variable which only serves to determine the optimal variation of the micro-texture amplitude. Its association with a physical signal will be considered in upcoming sections.

Thus far, it was sufficient to realize the target inputs just through time optimization, however for different scenarios time optimization by itself may not be sufficient to capture the targeted response i.e. target may be unrealizable. In the following sections, examples where space and geometry optimizations are needed to render such unrealizable cases will be presented.

6.2 Space Optimization

Spatial design variables allow different texture shapes to form during space optimization. In order to introduce the schematic, several results for space optimization are demonstrated in Figure 6.3. In these figures non-uniqueness is eminent because although the target traction is captured, the optimized textures do not necessarily display the target topology.

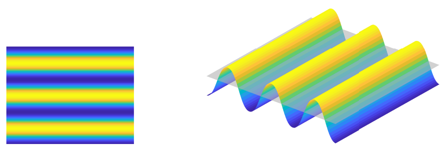

(a) target

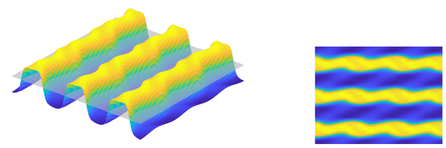

(b) optimized

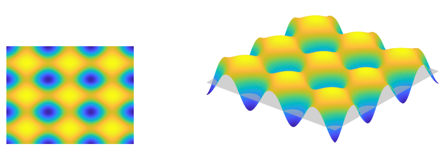

(c) target

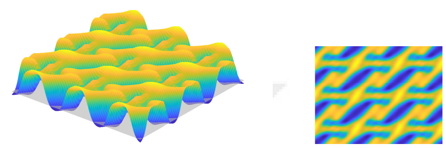

(d) optimized

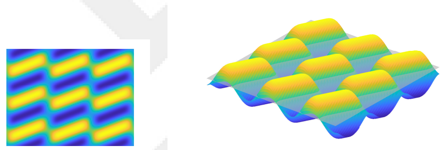

(e) target

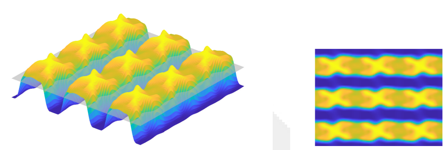

(f) optimized

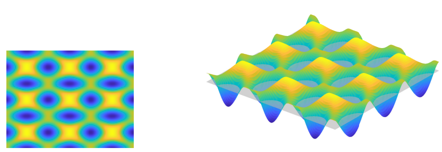

(g) target

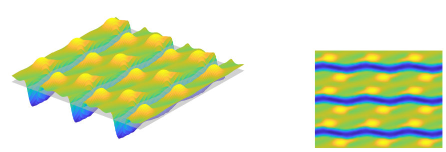

(h) optimized

Figure 6.3: *Target micro-textures provided to optimization algorithm are provided together with the optimized micro-textures which delivers the targeted macroscopic traction response. (a-b)* $H_{max} = 2.5$, $H_{min} = 0.1$, $\bar{h}^{+} = 1.2$, $\bar{h}^{-} = -1.2$, $h_0 = 1.3$, *(c-d)* $H_{max} = 2.5$, $H_{min} = 0.1$, $\bar{h}^{+} = 1.63$, $\bar{h}^{-} = -0.77$, $h_0 = 0.87$, *(e-f)* $H_{max} = 2.5$, $H_{min} = 0.1$, $\bar{h}^{+} = 1.2$, $\bar{h}^{-} = -1.2$, $h_0 = 1.3$, *(g-h)* $H_{max} = 2.5$, $H_{min} = 0.1$, $\bar{h}^{+} = 1.31$, $\bar{h}^{-} = -0.42$, $h_0 = 1.19$. *For all cases,* $\theta_G = 22.5°$, $\theta_V = 67.5°$. *In all optimized results traction matches with the target value with less than 1% error.*

In the overall optimization scheme, there are several reasons causing non-uniqueness in the designs. For space optimization, a reason of the non-uniqueness is due to the definition of objective function. To demonstrate this effect, an example for space optimization for targeted flux is given in Figure 6.4. For the assigned target micro-texture, objective is first written in terms of the square of the difference between targeted and the obtained flux for a single time step. This version is demonstrated in (6.1) as a special case of previously introduced objective function in (5.14)

$$\boldsymbol{\sigma}^{\boldsymbol{Q}} = \left(\sum_i \left(\frac{Q_i - Q_i^*}{Q_i^*} \right)^2 \right)^{\frac{1}{2}} . \tag{6.1a}$$

Subsequently, objective is built by using individual flow factor tensors as follows

$$\boldsymbol{\sigma}^{\boldsymbol{Q}} = \left(\sum_i \frac{(A_i - A_i^*)^2 + (C_i - C_i^*)^2}{(Q_i^*)^2} \right)^{\frac{1}{2}} . \tag{6.2a}$$

Both of these equations essentially describe the same target flux $\boldsymbol{Q}_i^*$. However in the second case this is done indirectly and more stringently by requiring that not only the flux components but all components of the flow factor tensors $\boldsymbol{A}$ and $\boldsymbol{C}$ match perfectly. Therefore, the micro-texture obtained via (6.2) look more alike to the target than the one obtained with (6.1). For an application where only realizable responses are desired and the target flow factors are known prior to optimization, an objective function that limits the system may be more preferable. However, for the most general scenario, an unknown target may be given which has a different $\boldsymbol{A}^*$, $\boldsymbol{C}^*$, $\boldsymbol{G}$ or $\boldsymbol{V}$ from the ones used to find the target flux which justifies the selection of (6.1).

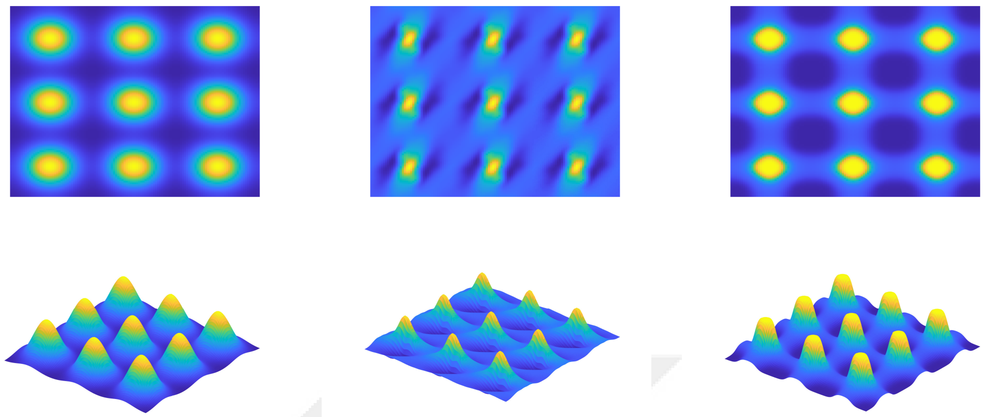

(a) target design (b) optimized design (6.1) (c) optimized design (6.2)

Figure 6.4: *Target vs optimized micro-textures by using different objectives to obtain same flux value is demonstrated.* $H_{max} = 1.9$, $H_{min} = 0.1$, $\bar{h}^{+} = 0.46$, $\bar{h}^{-} = -0.34$, $h_0 = 1.44$ $\theta_G = 0°$, $\theta_V = 45°$

For the following example in Figure 6.5, target is constructed by 45° $\boldsymbol{G}$ and $\boldsymbol{V}$, and with a sinusoidal micro-texture oriented again at 45°. When the same angles for $\boldsymbol{G}$ and $\boldsymbol{V}$ are given as an input, space optimization delivers a flux response with a high accuracy and a very similar micro-texture is formed as demonstrated in 6.5(e). However, one can assign angles of $\boldsymbol{G}$ and $\boldsymbol{V}$ that are not same as the target. In this case micro-texture adapts itself to deliver the target response. Figure 6.5 essentially demonstrates this adaptation of the micro-texture, thanks to space optimization. Yet, it is noted that if the optimization scheme and the target has different angles for $\boldsymbol{G}$ and $\boldsymbol{V}$, flux response cannot be obtained as well as the scenario where the angles are the same. This can be observed in Figure 6.5 where the optimized micro-textures with prescribed angles other than 45° for $\boldsymbol{G}$ and $\boldsymbol{V}$ cannot capture the target flux response. Therefore such targets appear to be unrealizable presently.

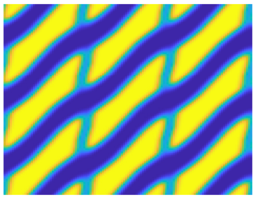

$\boldsymbol{G}$:0°, $\boldsymbol{V}$:0°
Q_1= -0.5136
Q_2= -0.5133

(a)

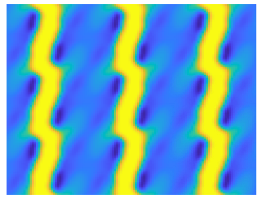

$\boldsymbol{G}$:0°, $\boldsymbol{V}$:45°
Q_1= 0.0396
Q_2= -0.5178

(b)

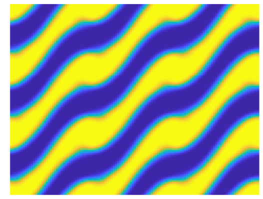

$\boldsymbol{G}$:0°, $\boldsymbol{V}$:90°
Q_1= -0.4840
Q_2= -0.5433

(c)

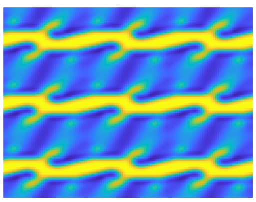

$\boldsymbol{G}$:45°, $\boldsymbol{V}$:0°
Q_1= -0.5107
Q_2= 0.0533

(d)

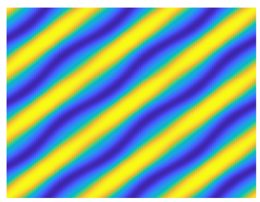

$\boldsymbol{G}$:45°, $\boldsymbol{V}$:45°
Q_1= -0.5201
Q_2= -0.5201

(e)

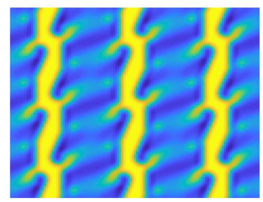

$\boldsymbol{G}$:45°, $\boldsymbol{V}$:90°
Q_1= -0.5426
Q_2= -0.4831

(f)

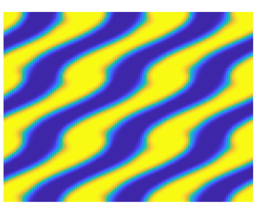

$\boldsymbol{G}$:90°, $\boldsymbol{V}$:0°
Q_1= -0.5426
Q_2= -0.4831

(g)

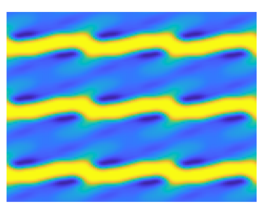

$\boldsymbol{G}$:90°, $\boldsymbol{V}$:45°
Q_1= -0.5128
Q_2= 0.0396

(h)

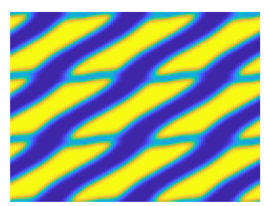

$\boldsymbol{G}$:90°, $\boldsymbol{V}$:90°
Q_1= -0.5135
Q_2= -0.5135

(i)

Figure 6.5: *Space optimization results are demonstrated for the targeted flux, generated with 45 degree sinusoidal grooves, $\theta_G = 45°$, $\theta_V = 45°$ and has the value of $Q_1 = -0.5142$, $Q_2 = -0.5142$. In all scenarios following quantities are kept the same: $H_{max} = 1.9$, $H_{min} = 0.1$, $\bar{h}^{+} = 0.9$, $\bar{h}^{-} = -0.9$, $h_0 = 1$*

Since space optimization enhances the design space by adopting the topography, results are expected to improve when time and space optimization are combined for an active texture response. In Figure 6.6, target flux is created by using a 45° grooved texture and space-time optimization is compared with the pure time optimization. For the time optimization, it is a necessity to assign a micro-texture because optimization finds only the time variation, as mentioned in the previous section. However, when the prescribed micro-texture has a different orientation than the target, adjusting the time variation is not sufficient by itself. In Figure 6.6, this is demonstrated by assigning a 0° grooved texture in a pure time optimization setting where the target has been prescribed to 45° groove micro-texture. Here, flux response is very well captured via space-time optimization, whereas for the time optimization the assigned target appears to be unrealizable. This visible improvement in the result demonstrates the capability of space-time optimization. Nonetheless, there may still be cases where space optimization cannot fully capture the targeted response. One of these cases was discussed for Figure 6.5; another one can be explained by the fixed unit cell which was employed in the calculations so far. This limitation is explained further in the next section.

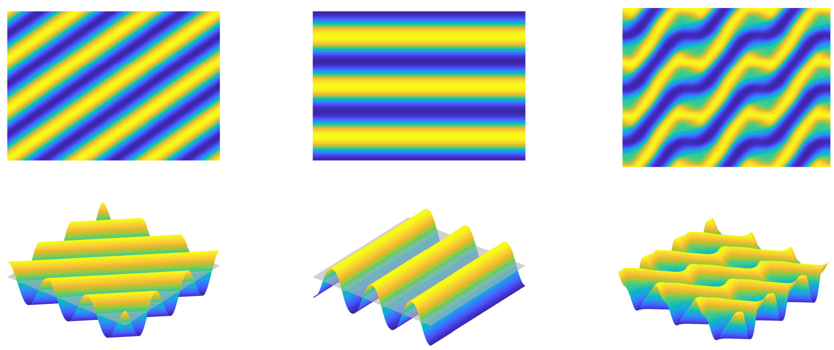

(a) target design

(b) assigned design for time optimization

(c) obtained design from space-time optimization

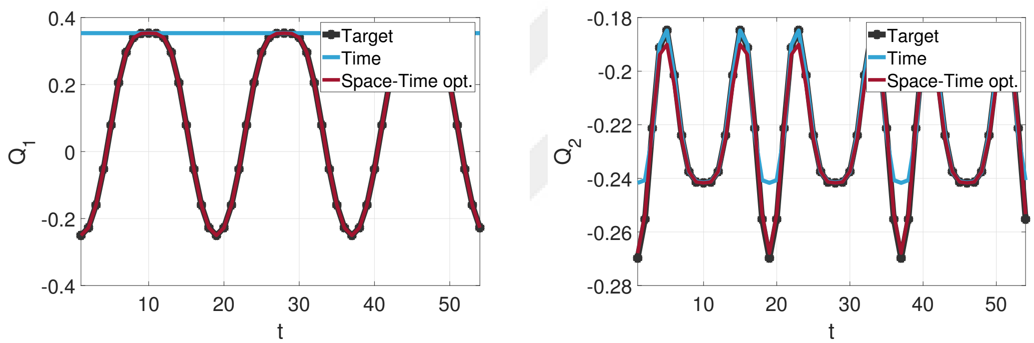

(d) macroscopic flux along x_1

(e) macroscopic flux along x_2

Figure 6.6: *Comparison of time optimization and space-time optimization for a targeted flux variation with* $H_{max} = 1.9$, $H_{min} = 0.1$, $\bar{h}^{+} = 0.9$, $\bar{h}^{-} = -0.9$, $h_0 = 1$.

6.3 Geometry Optimization

It is evident that space optimization improves the system response. However, design space is limited with a fixed unit cell geometry, that is typically chosen as a square. As a particular example, when the grooves of a microtexture are oriented along an angle such as 20°, space optimization may not find the optimal micro-texture for the targeted response because the cell geometry restricts the development of the distribution. In order to circumvent this suboptimality, geometry optimization is added to the framework within which the unit cell can adjust its shape during the optimization.

In Figure 6.7, combination of space and geometry optimization is compared with the pure space optimization for a single time step to exemplify the improvement due to geometry optimization. Target is assigned to be a 20° rotated unit cell, which is the same as assigning a fixed unit cell with 20° rotated grooves. In order to capture the targeted flux response, first space optimization is employed in Figure 6.7(b). However, space optimization itself clearly cannot obtain targeted flux with a fixed unit cell. Afterwards, geometry optimization is activated in addition to space optimization and the unit cell is allowed to adjust its shape as demonstrated in 6.7(c). It is observed that although peaks and valleys form in the space optimization in 6.7(b), angle of the target cannot be captured exactly. On the other hand, geometry adaptation allows unit cell to rotate and eventually obtain the exact target response with a 20° angle.

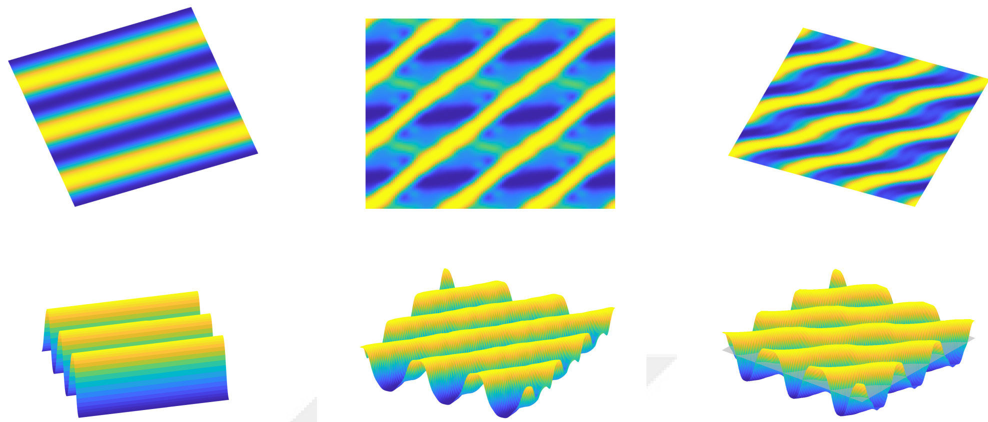

Target	Space Optimization	Space and Geometry Optimization
Q_1 = -0.3910	Q_1 = -0.2226	Q_1 = -0.3886
Q_2 = -0.1448	Q_2 = -0.2565	Q_2 = -0.1442
(a)	(b)	(c)

Figure 6.7: *Micro-texture comparisons for macroscopic flux responses for a target that rotated* $20°$. $H_{max} = 1.9$, $H_{min} = 0.1$, $\bar{h}^{+} = 0.9$, $\bar{h}^{-} = -0.9$, $h_0 = 1$ $\theta_G = 22.5°$, $\theta_V = 67.5°$

6.4 Geometry-Space-Time Optimization

Having introduced the individual optimization features, this section demonstrates systematic improvement in optimization when more and more of these features are incorporated. Therefore for each figure time, space-time and space-time-geometry optimization results are presented. For the examples, realizable and unrealizable targets are chosen for both flux- and traction-based objectives.

In Figure 6.8, target flux is created using a $20°$ rotated unit cell with grooved micro-texture which was demonstrated in figures 6.7(a) and a time dependent change is visualized for the target in figures 6.8(d) and 6.8(e). For the time optimization, a $0°$ micro-texture is assigned which predictably cannot obtain the target flux response. Subsequently, space optimization is added to the system which enhances the results but still cannot fully capture the target. Finally when all three optimization schemes run together, target is rendered fully realizable and accurately captured.

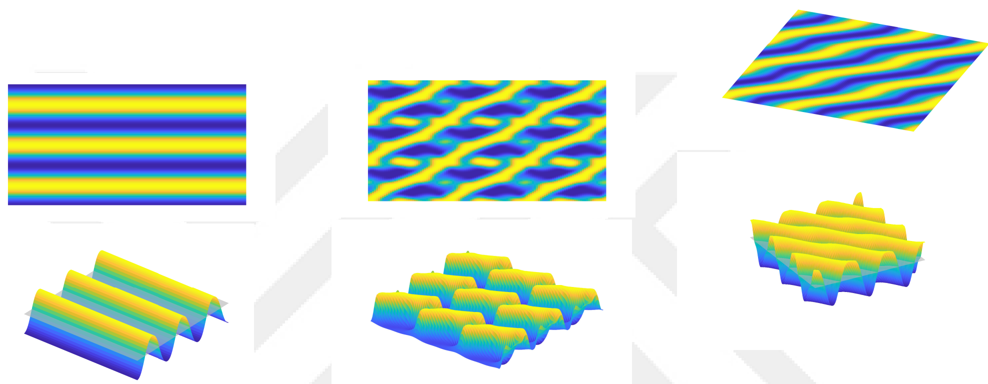

assigned micro-texture for time optimization

(a)

obtained micro-texture from space-time optimization

(b)

obtained micro-texture from space-time-geometry optimization

(c)

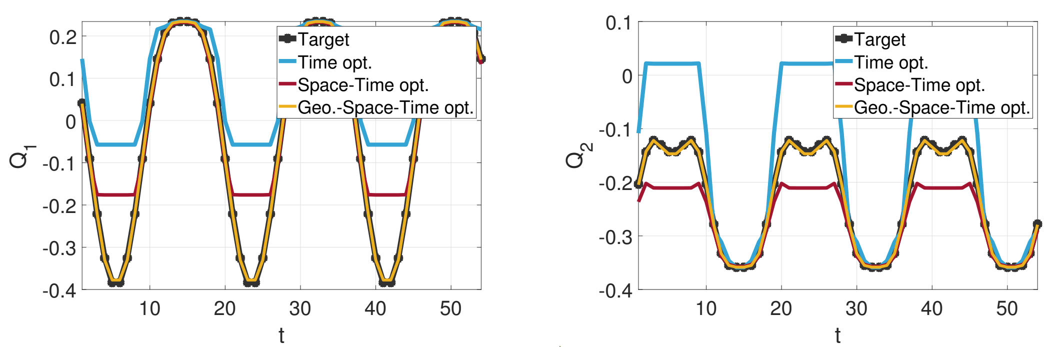

(d) Macroscopic flux along x_1

(e) Macroscopic flux along x_2

Figure 6.8: *Systematic improvability in optimization with an increasing number of optimization features is demonstrated for a realizable flux response. Objective values at the converged system are: 0.331739 for time, 0.084718 for space-time and 0.000102 for the space-time-geometry optimization.* $H_{max} = 1.9$, $H_{min} = 0.1$, $\bar{h}^+ = 0.9$, $\bar{h}^- = -0.9$, $h_0 = 1$ $\theta_G = 22.5°$, $\theta_V = 67.5°$

The 20° rotated grooved micro-texture is also used to create a target for the traction example in Figure E.3. Contrary to example in Figure 6.8, in this example both space-time and geometry-space-time optimization options delivered an accurate result and captured the signal. Therefore, it is noted that as long as a target is attainable with any combination of the optimization schemes, it can be classified as realizable. Also, it is noted that typically the target is indistinguishable from the optimization result once the optimization function falls below 10^{-2}.

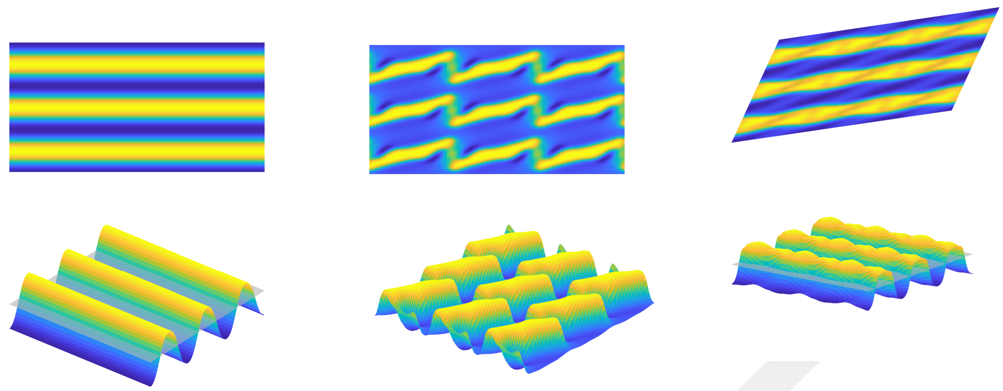

assigned micro-texture for time optimization

(a)

obtained micro-texture from space-time optimization

(b)

Obtained micro-texture from space-time-geometry optimization

(c)

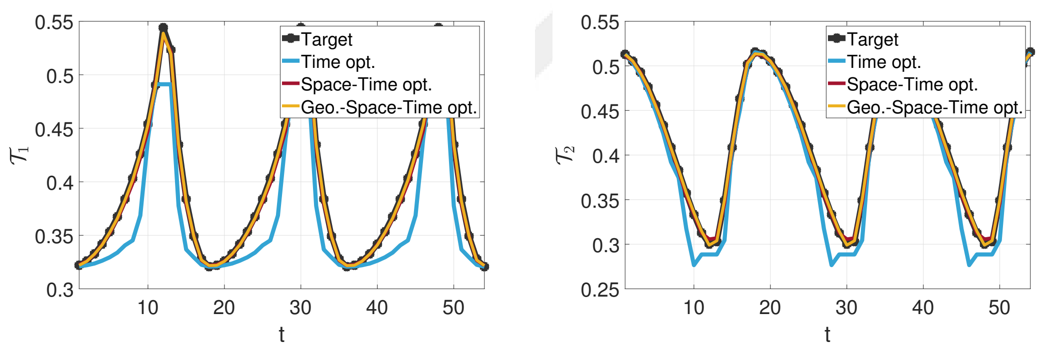

(d) macroscopic traction along x_1

(e) macroscopic traction along x_2

Figure 6.9: *Systematic improvability in optimization with an increasing number of optimization features is demonstrated for a realizable traction response. Objective values at the converged system are: 0.010458 for time, 0.000088 for space-time and 0.000022 for the space-time-geometry optimization.* $H_{max} = 1.9$, $H_{min} = 0.1$, $\bar{h}^{+} = 0.9$, $\bar{h}^{-} = -0.9$, $h_0 = 1$ $\theta_G = 22.5°$, $\theta_V = 67.5°$

For the second type of examples, the flux or traction is evaluated based on $\boldsymbol{G}$ and $\boldsymbol{V}$ values which differ from those with which the target flux or traction was generated from a prescribed micro-texture. This will effectively render the targets unrealizable. A similar scenario was created before in Figure 6.5 to test the capability of the space optimization.

As it is apparent in both Figure 6.10 and Figure 6.11, addition of each optimization to the system improves the optimization outcome and provides an increasingly closer match to the targeted response despite the fact that target can never be obtained one-to-one. Here, changing the orientations of $\boldsymbol{G}$ and $\boldsymbol{V}$ is observed to render the targets unrealizable for all combinations of optimization options. However, this is not the only way to create unrealizable targets. Other options are: different maximum and/or minimum film thickness than the optimization scheme, a linear transformation for the unit cell which cannot be reached with the assigned interval to $\boldsymbol{P}$ in the optimization scheme and a non-periodic time signal (in the presence of time filter). These additional options will not be discussed further.

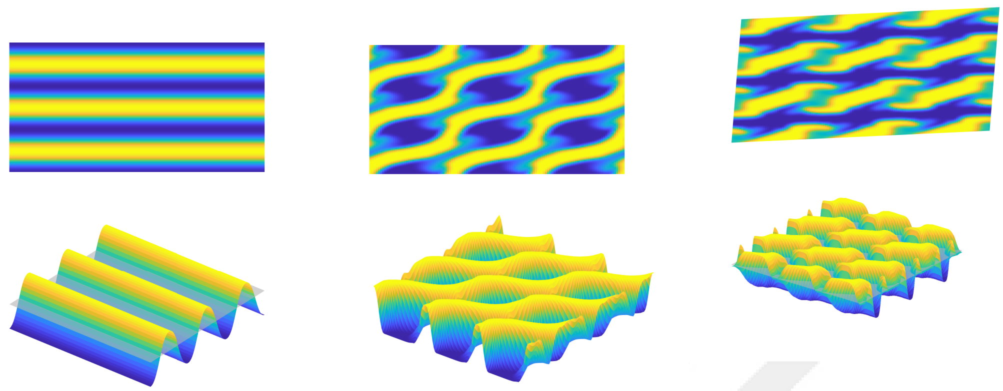

assigned micro-texture for time optimization

(a)

obtained micro-texture from space-time optimization

(b)

obtained micro-texture from space-time-geometry optimization

(c)

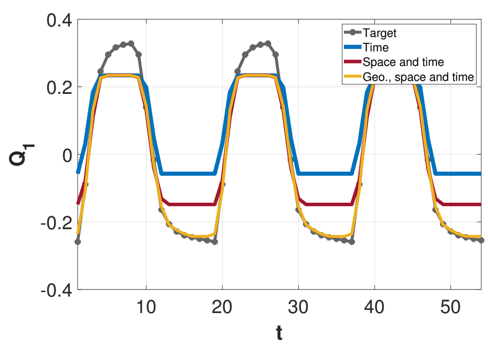

(d) Macroscopic flux along x_1

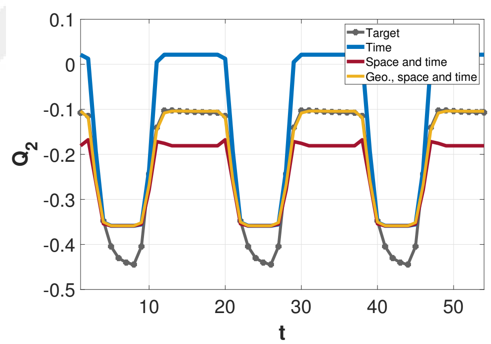

(e) Macroscopic flux along x_2

Figure 6.10: *Systematic improvability in optimization with an increasing number of optimization features is demonstrated for a unrealizable flux response. Objective values at the converged system are: 0.268818 for time, 0.088203 for space-time and 0.0026026 for the space-time-geometry optimization.* $H_{max} = 1.9$, $H_{min} = 0.1$, $\bar{h}^{+} = 0.9$, $\bar{h}^{-} = -0.9$, $h_0 = 1$ $\theta_G = 22.5°$, $\theta_V = 67.5°$

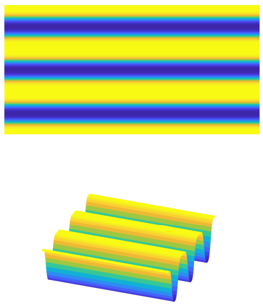

Assigned micro-texture for time optimization

(a)

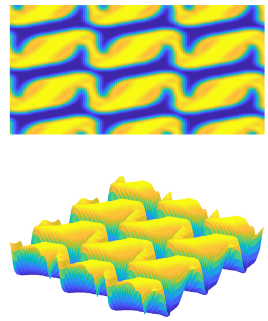

Obtained micro-texture from space-time optimization

(b)

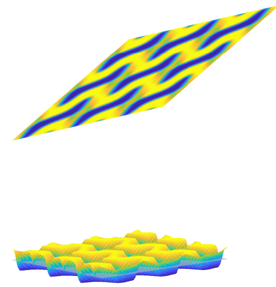

Obtained micro-texture from space-time-geometry optimization

(c)

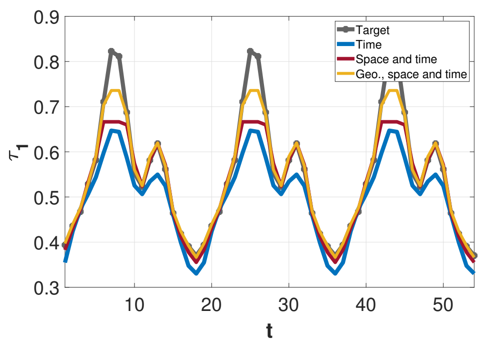

(d) macroscopic traction along x_1

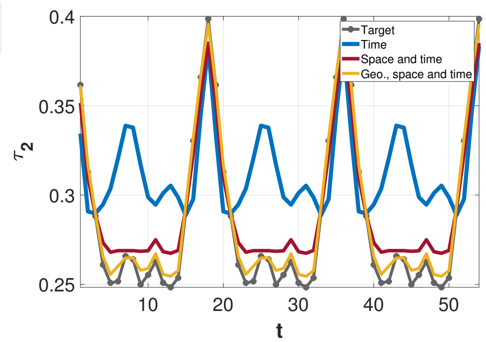

(e) macroscopic traction along x_2

Figure 6.11: *Systematic improvability in optimization with an increasing number of optimization features is demonstrated for a unrealizable traction response. Objective values at the converged system are: 0.031926 for time, 0.005902 for space-time and 0.001389 for the space-time-geometry optimization.* $H_{max} = 1.9$, $H_{min} = 0.1$, $\bar{h}^{+} = 0.9$, $\bar{h}^{-} = -0.9$, $h_0 = 1$ $\theta_G = 22.5°$, $\theta_V = 67.5°$

Chapter 7

Three-Dimensional Realization

In this chapter, 3D realization for the optimization results are demonstrated. The results which are obtained from topology optimization are projected on a 3D active material and the temporal change is associated with the electric voltage.

7.1 Material Design

In order to demonstrate an example for the usage of topology optimization in an application, a recently proposed material design for the active surfaces is employed [1, 8]. The proposed system consists of an elastomer which has a continuous electrode on the upper surface and an electrode distribution at the bottom fixed surface as depicted in the Figure 7.1(a). When a voltage is applied to the electrodes, they pull each other which deforms the underlying material, thereby generating a surface texture. Based on this principle, the idea is to determine the shape and distribution of the electrodes and the voltage variation so that the results of topology optimization can be replicated. Such 3D realizations of active surfaces will be presented in this section.

In the most general setting possible for the described problem, a fully coupled electroelasticity problem should be solved where one would carry out the optimization considering the time dependent deformation of the 3D model. Such a problem would require the computation of surface texture variation at each time step and would be very expensive computationally. A critical step adopted in this work is therefore to simplify such an expensive coupling by assuming that the amplitude for the surface texture, i.e. $\bar{h}$, is independent of the applied voltage. Note that the independence of $\bar{h}$ from the external signal i.e. τ, had already been assumed in the optimization framework as well. Therefore, retaining this decoupling, once the surface topology is established by the optimization algorithm, it is sufficient to project the result and find the voltage variation which is associated with τ. In order to solve relevant electroelasticity problem, FE framework is be employed based on COMSOL Multiphysics [59]. The electrostatics and the elasticity parts of the problem will be discussed separately in the following sections.

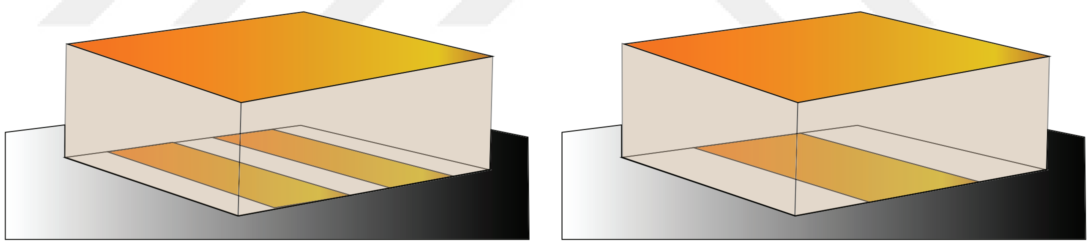

(a) Double electrode (b) Single electrode

Figure 7.1: *The adapted material design is demonstrated as a double and a single electrode unit cells. (a) Previously proposed model by [1] where potentials of the two electrodes at the bottom oscillates with opposite voltages while the upper electrode preserves its value; so that an inverting sinusoidal shapes develops at the surface. (b) The model used in this study, upper surface is pulled when upper and lower electrodes are oppositely charged, and released for no voltage is applied; no inversion is observed.*

7.2 Electrostatics Problem

Assigned voltages on the electrodes create an electric field over the domain and a charge density piles up on the electrodes. As indicated in [1], electrodes are much thinner than the elastomer. Therefore in the FE model they are simply represented by a surface on which voltage is applied. Additionally, the surrounding environment is eliminated from the model as a further simplification (see Appendix C for both simplifications). In order to solve the electrostatic problem, Gauss's law is utilized as the equilibrium equation which reads

$$\nabla \cdot \epsilon_0 \boldsymbol{E} = \rho \tag{7.1}$$

where ϵ_0 is the permittivity of the free space, $\boldsymbol{E}$ is the electric field and ρ is the total charge density. Here, total charge density ρ is the sum of free charges ρ_f, which develop independent of the medium, and bound charges ρ_b which occur due to the dielectric medium of the elastomer:

$$\rho = \rho_f + \rho_b. \tag{7.2}$$

Bound charges are associated with polarization, denoted by $\boldsymbol{P}$, i.e. $\rho_b = -\nabla \cdot \boldsymbol{P}$ within the domain and surface bound charges via $\sigma_b = -\boldsymbol{P} \cdot \boldsymbol{n}$ on the boundary. Using these terms, Gauss's law for the dielectrics is rewritten as

$$\nabla \cdot (\epsilon_0 \boldsymbol{E}) = \rho_f + \rho_b = \rho_f - \nabla \cdot \boldsymbol{P} \quad . \tag{7.3}$$

Since free charges develop independent of the environment, it is convenient to only work with ρ_f by combining divergence terms and expressed the Gauss's law in the alternative form

$$\nabla \cdot (\epsilon_0 \boldsymbol{E} + \boldsymbol{P}) = \rho_f \quad . \tag{7.4}$$

Based on this form, the electric displacement field is defined as

$$\boldsymbol{D} = \epsilon_0 \boldsymbol{E} + \boldsymbol{P} \quad . \tag{7.5}$$

For linear dielectrics, polarization is proportional to the electric field via permittivity of the free space and electric susceptibility, χ, with $\boldsymbol{P} = \epsilon_0 \chi \boldsymbol{E}$ where χ

depends on the microscopic structure of the material medium. Employing this relation in (7.4), and defining relative permittivity as $\epsilon_r = 1 + \chi$, one obtains

$$\nabla \cdot (\epsilon_0 \epsilon_r \boldsymbol{E}) = \rho_f. \tag{7.6}$$

This form of the Gauss's law is preferred over (7.1) because it gives reference to only ρ_f, which can be controlled, instead of the bound charges [60]. The relative permittivity ϵ_r is known for commonly used materials and taken as 2.7 for the chosen PDMS material [1]. Noting that the electric field equals to the gradient of electric potential, $\boldsymbol{E} = -\nabla V$, electrodes are assigned opposite voltages $\pm V_0$ as boundary conditions, and $\rho_f = 0$ is assigned within the domain. Additionally, reciprocal faces of the unit cell are subjected to periodic boundary condition.

7.3 Solid Mechanics Problem

In order to find the deformation, equilibrium equation reads

$$\nabla \cdot \boldsymbol{T} + \boldsymbol{f} = 0 \tag{7.7}$$

should be solved where $\boldsymbol{T}$ is Cauchy stress tensor and $\boldsymbol{f}$ is the body force per unit volume. Note that in an electroelasticity setting, both $\boldsymbol{T}$ and $\boldsymbol{f}$ depend on deformation and the electrostatics fields. Moreover $\boldsymbol{T}$ is in general not symmetric and depends on both the deformation and the electrostatics field [61]. It will be assumed that tractions which are generated due to charge accumulation of the electrodes on the top surface dominates the mechanical response. Hence, as a first level of approximation, it is assumed that $\boldsymbol{f} = \boldsymbol{0}$ and that $\nabla \boldsymbol{T}$ depends only on deformation. The boundary conditions which are applied to this purely mechanical problem are primarily associated with tractions t_a which are generated due to the surface total charge density σ_s accumulation on the electrodes:

$$\mathbf{t_a} = \sigma_\mathbf{s} \boldsymbol{E}. \tag{7.8}$$

Here, σ_s is determined from the jump of the electric field from outside of the material to the inside across the boundary:

$$\sigma_s = \epsilon_0 (E^{\perp}_{out} - E^{\perp}_{in}) = \epsilon_0 [\![\boldsymbol{E} \cdot \boldsymbol{n}]\!]. \tag{7.9}$$

Note that, there is no electric field outside of the material for the upper surface where the traction is applied, therefore $E^{\perp}_{out} = 0$. In addition, this boundary condition can be re-expressed as

$$\sigma_s = \epsilon_r^{-1}(D^{\perp}_{out} - D^{\perp}_{in}) = \epsilon_r^{-1}[\![\boldsymbol{D} \cdot \boldsymbol{n}]\!] \tag{7.10}$$

for linear dielectric materials, which is the version used in this study. For representing a unit cell, periodic boundary conditions are given to lateral sides of the unit cell and the bottom face is given fixed boundary condition.

Neo-Hookean hyperleastic model is selected to model the PDMS material between the electrodes. This material has a very large Poisson ratio and therefore is assumed to be incompressible. The deviatoric strain energy function takes the form

$$w^{dev} = \frac{1}{2}G(J^{-\frac{2}{3}}tr(\boldsymbol{C}) - 3) \tag{7.11}$$

where G is the shear modulus, $J = det(\boldsymbol{F})$ is the jacobian of the deformation gradient $\boldsymbol{F}$, and $\boldsymbol{C}$ is the right Cauchy-Green deformation tensor. The Second Piola-Kirchhoff stress is may be expressed from the derivative of the strain energy density

$$\boldsymbol{S}^{dev} = \frac{\partial w^{dev}}{\partial \boldsymbol{C}} = GJ^{-\frac{2}{3}}(\boldsymbol{I} - \frac{1}{3}tr(\boldsymbol{C})\boldsymbol{C}^{-1}). \tag{7.12}$$

Consequently, Cauchy stress $\boldsymbol{T} = \frac{1}{J}\boldsymbol{F}\boldsymbol{S}\boldsymbol{F}^T$ is obtained and implemented in (7.7)

$$\boldsymbol{T}^{dev} = GJ^{-\frac{5}{3}}\boldsymbol{b}^{dev} \tag{7.13}$$

where $\boldsymbol{b}^{dev}$ is the deviatoric part of the left Cauchy-Green deformation tensor. The pressure contribution which results from the incompressibility constraint is not explicitly shown.

7.4 Parameter Selections

In this section, selected parameters for the 3D model are discussed in detail which are the deformation amplitude, applied voltage, size and the shape of mesh for the 3D unit cell.

The experimental basis for this setup employed lower voltages which let to lower surface deformation on the order of $100\,nm$. Consequently higher voltages will need to be applied presently to achieve target deflections. Additionally, for a given voltage, the extent of the deformation depends on the thickness of the dielectric medium. For high voltages and low thickness values, one starts to violate the assumption that $\bar{h}$ is independent of the external signal. To avoid this, a sufficiently large thicknesses is required and presently will be chosen as $20\,\mu m$. Similarly, although homogenization is insensitive to the lateral dimensions, the lateral dimensions are important for the context of electroelasticity. Here, an absolute value of $40\,\mu m$ is chosen for both lateral dimensions of the unit cell. Considering that the chosen average film thicknesses h_0 is of the order of $1\mu m$, this choice additionally ensures the validity of the Reynolds roughness regime that has been assumed within the homogenization framework [51].

Numerically, the shape of the mesh might influence the result for the deformation at course resolutions. It is observed that a uniform mesh delivers more smooth structures (see Appendix D). Finally, the reference design consists of oppositely charged parallel electrodes at the bottom of the elastomer Figure 7.1(a). This design allows the texture to invert the peaks and valleys when the bottom electrodes exchange their voltage signs. This kind of a texture application can be obtained by the optimization framework when the temporal design variable τ is allowed to run through negative values. However, this will not be pursued in this study (see Appendix E).

7.5 Micro-Texture Projection

In order to find the distribution of the electrodes, the results from topology optimization are used. However, since the obtained results describe a smooth surface variation, they do not show a clear description of where electrodes could be placed in order to attain such a topology. For this purpose, a straightforward projection method is proposed where the domain is separated into two parts: one part where the film thickness is above h_0 and the remaining part where it is lower.

Subsequently, one of them is chosen as the region where the electrodes are placed. In the following discussion, a case study is considered with this projection that is depicted in Figure 7.2(b).

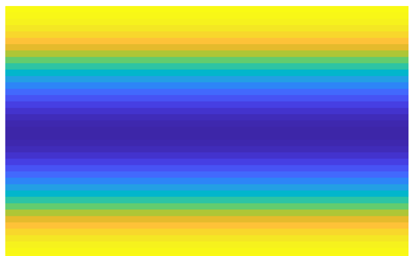

(a) Assigned microstructure

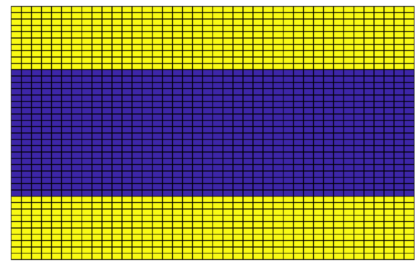

(b) Assigned microstructure

Figure 7.2: *Microtexture of the topology optimization is given on the rigth, and its projection is given on the left*

Note that, for a double electrode system, the surface cannot be divided into strictly two subdomains, but require a transitional are which is not discussed here (see Appendix F).

7.6 Case Study

Flux optimization example in chapter 6.1 is chosen and the projection shown in Figure 7.2(b) is employed. In this example, the microstructure is known. Therefore, only the temporal variation τ is correlated with the voltage change. Accordingly, the maximum deflections obtained from topology optimization for each time step are compared with the deflections obtained from the 3D model. In the chosen topology optimization result, h^+ and h^- were assumed to be equal at each time step. However, due to nonlinear behavior of the material, it is challenging to obtain such a symmetry in the 3D realization application. The incompressible material model ensures that the average does not change, however the magnitudes of the minimum and maximum deviations from the average grows more and more different as the voltage increases. Nevertheless, it will be observed that the 3D realization delivers a surface texture which induces a macroscopic response that closely follows the target.

After the required voltages are determined for each time step, the resultant deformation of the upper surface of the 3D model is projected back into the homogenization framework and the results are compared. In Figure 7.3, the lubrication response of the modeled surface is compared with the previously demonstrated target and topology optimization results. The temporal design variable τ is additionally associated with the voltage variation in figure 7.3(c). The excellent match between the two sets of results demonstrates the feasibility of the overall optimization framework.

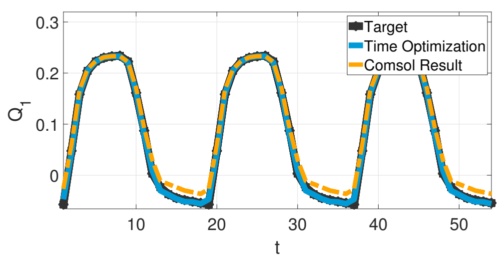

(a) Macroscopic Flux on x_1

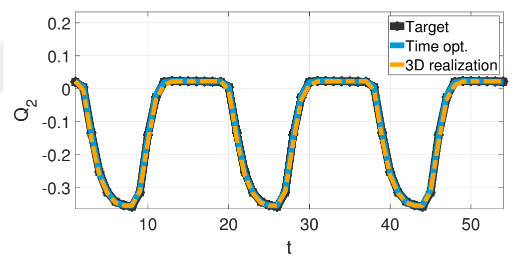

(b) Macroscopic Flux on x_2

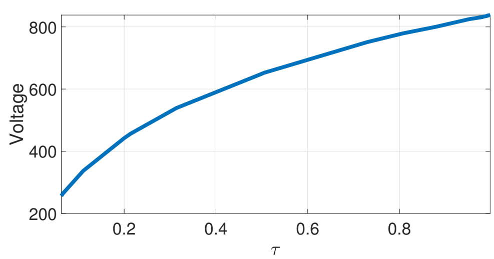

(c) τ vs voltage

Figure 7.3: *Macroscopic flux due to the temporal variation of the surface for target, optimization result and 3D model model is compared. Variable τ is associated with the applied voltage which causes deformation in the unit cell.*

The deformation as the voltage is increased is additionally demonstrated in Figure 7.4. Unit cell surface deforms to a sinusoidal shape with the increased voltage and comes back to its undeformed shape when the voltage is released.

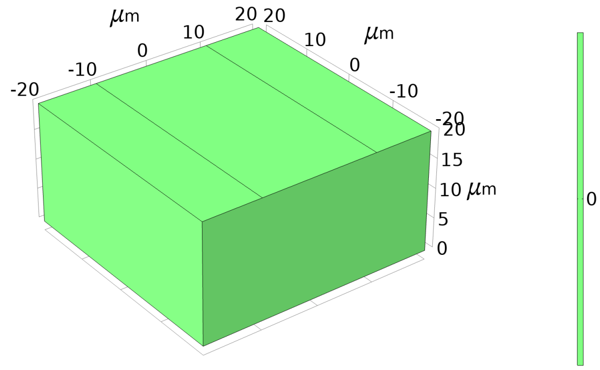

(a) 0V

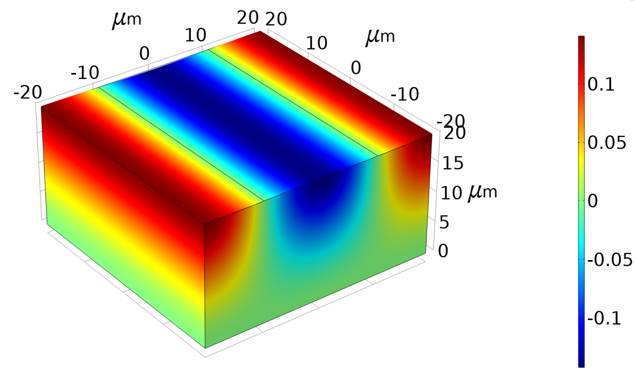

(b) 400V

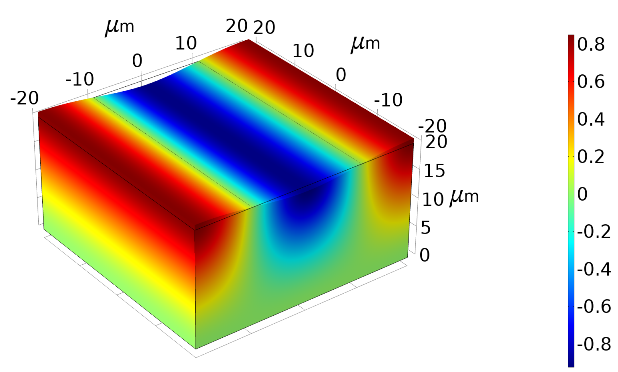

(c) 924V

Figure 7.4: *Deformation of the surface is demonstrated in the* x_3 *direction where (a) there is no deformation, (b) approximately* $0.15\mu m$ *deformation and (c) maximum amount of deformation applied in the case study.*

Chapter 8

Conclusion

In this study, active micro-texture design is introduced by employing a homogenization-based topology optimization framework for hydrodynamic lubrication. For the lubrication problem, multiscale analysis is applied via scale seperation and homogenized coefficients for the macroscopic response are obtained. Within a gradient-based optimization algorithm, sensitivities of the effective macroscopic quantities are introduced to the optimization algorithm. Both spatial and temporal variations of a micro-texture are established for target flux or traction responses. In addition, a geometry optimization concept is introduced for adjusting the shape of unit cell to circumvent suboptimal results due to a fixed geometry. It is observed that each optimization feature enhances the design space to some extent. For both realizable and unrealizable cases, the best results are obtained when all optimization features are activated. Afterwards, the obtained results from topology optimization are employed to construct a 3D model for the texture, utilizing an experimental setup. The effective lubrication responses for the target, optimization outcomes and the 3D realization are compared and verified to be in a good agreement. The presented framework introduces topology optimization as a methodology to design active micro-textures and it has the advantage of computational efficiency due to the decoupling of the optimization and the 3D realization stages. Note that although the adaptation of topology optimization results are studied on a elastomer-electrode based tunable material architecture, it has the potential to be adopted in other applications as well. This work introduces a strategy by employing topology optimization for the active material design which may be adapted in fields other than hydrodynamic lubrication.

This study assumes Reynolds regime. Depending on the wavelength of the surface design features and the film thickness, extension of the framework towards to Stokes regime may be necessary. Additionally, for the 3D realization of the active surface, this study utilized the assumption of decoupling among the electrostatic and elasticity problems. This assumption simplifies the 3D realization yet the investigation of a fully coupled analysis is necessary to assess its validity.Further research along these items will help achieve micro-texture design frameworks with improved physical reliability.

Bibliography

[1] F. L. Visschers, H. Gojzewski, G. J. Vancso, D. J. Broer, and D. Liu, "Oscillating surfaces fueled by a continuous ac electric field," *Advanced Materials Interfaces*, vol. 6, no. 21, p. 1901292, 2019.

[2] K. Chen, X. Yang, G. Lv, Y. Zhang, H. Yang, and Y. Gao, "Research progress of surface modification and solid–liquid lubrication synergistic friction reduction and wear resistance," *The International Journal of Advanced Manufacturing Technology*, vol. 122, no. 3-4, pp. 1115–1141, 2022.

[3] B. Bhushan, *Introduction to tribology.* John Wiley Sons, 2013.

[4] B. J. Hamrock, B. J. Schmid, and B. O. Jacobson, *Fundamentals of fluid film lubrication*, vol. 169. CRC press, 2004.

[5] D. Gropper, L. Wang, and T. J. Harvey, "Hydrodynamic lubrication of textured surfaces: A review of modeling techniques and key findings," *Tribology International*, vol. 94, pp. 509–529, 2016.

[6] S. K. Leist, D. Gao, R. Chiou, and J. Zhou, "Investigating the shape memory properties of 4d printed polylactic acid (PLA) and the concept of 4d printing onto nylon fabrics for the creation of smart textiles," *Virtual and Physical Prototyping*, vol. 12, no. 4, pp. 290–300, 2017.

[7] Y. Kim, H. Yuk, R. Zhao, S. A. Chester, and X. Zhao, "Printing ferromagnetic domains for untethered fast-transforming soft materials," *Nature*, vol. 558, no. 7709, pp. 274–279, 2018.

[8] F. L. Visschers, D. J. Broer, and D. Liu, "Programmed topographical features generated on command in confined electroactive films," *Soft Matter*, vol. 17, no. 31, pp. 7247–7251, 2021.

[9] W. "Miao, W. Zou, B. Jin, C. Ni, N. Zheng, Q. Zhao, and T. Xie, "On demand shape memory polymer via light regulated topological defects in a dynamic covalent network," *Nature Communications*, vol. 11, no. 1, p. 4257, 2020.

[10] P. Giusto, B. Kumru, J. Zhang, R. Rothe, and M. Antonietti, "Let a hundred polymers bloom: tunable wetting of photografted polymer-carbon nitride surfaces," *Chemistry of Materials*, vol. 32, no. 17, pp. 7284–7291, 2020.

[11] Y. Zhan, W. Li, A. Amirfazli, and S. Yu, "Recent advances in shape memory superhydrophobic surfaces: Concepts, mechanism, classification, applications and challenges," *Polymer*, p. 125193, 2022.

[12] S. Lampaert and R. Van Ostayen, "Experimental results on a hydrostatic bearing lubricated with a magnetorheological fluid," *Current Applied Physics*, vol. 19, no. 12, pp. 1441–1448, 2019.

[13] I. F. Santos, "Controllable sliding bearings and controllable lubrication principles—an overview," *Lubricants*, vol. 6, no. 1, p. 16, 2018.

[14] M. Murashima, Y. Imaizumi, R. Murase, N. Umehara, T. Tokoroyama, T. Saito, and M. Takeshima, "Active friction control in lubrication condition using novel metal morphing surface," *Tribology International*, vol. 156, p. 106827, 2021.

[15] M. Fesanghary and M. Khonsari, "On the shape optimization of self-adaptive grooves," *Tribology Transactions*, vol. 54, no. 2, pp. 256–264, 2011.

[16] C. Shen and M. Khonsari, "Numerical optimization of texture shape for parallel surfaces under unidirectional and bidirectional sliding," *Tribology International*, vol. 82, pp. 1–11, 2015.

[17] A. Ramesh, W. Akram, S. P. Mishra, A. H. Cannon, A. A. Polycarpou, and W. P. King, "Friction characteristics of microtextured surfaces under mixed

and hydrodynamic lubrication," *Tribology International*, vol. 57, pp. 170–176, 2013.

[18] W. Wang, Y. He, J. Zhao, J. Mao, Y. Hu, and J. Luo, "Optimization of groove texture profile to improve hydrodynamic lubrication performance: Theory and experiments," *Friction*, vol. 8, pp. 83–94, 2020.

[19] N. Morris, M. Leighton, M. De la Cruz, R. Rahmani, H. Rahnejat, and S. Howell-Smith, "Combined numerical and experimental investigation of the micro-hydrodynamics of chevron-based textured patterns influencing conjunctional friction of sliding contacts," *Proceedings of the Institution of Mechanical Engineers, Part J: Journal of Engineering Tribology*, vol. 229, no. 4, pp. 316–335, 2015.

[20] M. Uddin, T. Ibatan, and S. Shankar, "Influence of surface texture shape, geometry and orientation on hydrodynamic lubrication performance of plane-to-plane slider surfaces," *Lubrication Science*, vol. 29, no. 3, pp. 153–181, 2017.

[21] K. Yagi, W. Matsunaka, and J. Sugimura, "Impact of textured surfaces in starved hydrodynamic lubrication," *Tribology International*, vol. 154, p. 106756, 2021.

[22] Q. Guo, L. Zheng, Y. Zhong, S. Wang, and L. Ren, "Numerical simulation of hydrodynamic lubrication performance for continuous groove-textured surface," *Tribology International*, vol. 167, p. 107411, 2022.

[23] L. Rayleigh, "I. notes on the theory of lubrication," *The London, Edinburgh, and Dublin Philosophical Magazine and Journal of Science*, vol. 35, no. 205, pp. 1–12, 1918.

[24] S. Rohde and G. McAllister, "On the optimization of fluid film bearings," *Proceedings of the Royal Society of London. A. Mathematical and Physical Sciences*, vol. 351, no. 1667, pp. 481–497, 1976.

[25] R. A. Van Ostayen, "Film height optimization of dynamically loaded hydrodynamic slider bearings," *Tribology international*, vol. 43, no. 10, pp. 1786–1793, 2010.

[26] S. F. Alyaqout and A. A. Elsharkawy, "Optimal film shape for two-dimensional slider bearings lubricated with couple stress fluids," *Tribology International*, vol. 44, no. 3, pp. 336–342, 2011.

[27] G. Zhang, J. Li, Z. Tian, Y. Huang, and R. Chen, "Film shape optimization for two-dimensional rough slider bearings," *Tribology Transactions*, vol. 59, no. 1, pp. 17–27, 2016.

[28] H. Hashimoto and M. Ochiai, "Optimization of groove geometry for thrust air bearing to maximize bearing stiffness," 2008.

[29] C. Shen and M. Khonsari, "Texture shape optimization for seal-like parallel surfaces: theory and experiment," *Tribology Transactions*, vol. 59, no. 4, pp. 698–706, 2016.

[30] A. Waseem, İ. Temizer, J. Kato, and K. Terada, "Homogenization-based design of surface textures in hydrodynamic lubrication," *International Journal for Numerical Methods in Engineering*, vol. 108, no. 12, pp. 1427–1450, 2016.

[31] A. Waseem, İ. Temizer, J. Kato, and K. Terada, "Micro-texture design and optimization in hydrodynamic lubrication via two-scale analysis," *Structural and Multidisciplinary Optimization*, vol. 56, pp. 227–248, 2017.

[32] H. Zhang, G.-n. Dong, M. Hua, and K.-S. Chin, "Improvement of tribological behaviors by optimizing concave texture shape under reciprocating sliding motion," *Journal of Tribology*, vol. 139, no. 1, p. 011701, 2017.

[33] H. Zhang, M. Hua, G.-z. Dong, D.-y. Zhang, W.-j. Chen, and G.-n. Dong, "Optimization of texture shape based on genetic algorithm under unidirectional sliding," *Tribology International*, vol. 115, pp. 222–232, 2017.

[34] X. Wang, L. Shi, Q. Dai, W. Huang, and X. Wang, "Multi-objective optimization on dimple shapes for gas face seals," *Tribology International*, vol. 123, pp. 216–223, 2018.

[35] B. A. Çakal, İ. Temizer, K. Terada, and J. Kato, "Microscopic design and

optimization of hydrodynamically lubricated dissipative interfaces," *International Journal for Numerical Methods in Engineering*, vol. 120, pp. 153–178, 2019.

[36] Y. Yu, G. Pu, T. Jiang, and K. Jiang, "Discontinuous grooves in thrust air bearings designed with capso algorithm," *International Journal of Mechanical Sciences*, vol. 165, p. 105197, 2020.

[37] T. Zhirong, M. Xiangkai, M. Yi, and P. Xudong, "Shape optimization of hydrodynamic textured surfaces for enhancing load-carrying capacity based on level set method," *Tribology International*, vol. 162, p. 107136, 2021.

[38] Q. Guo, L. Zheng, Y. Zhong, S. Wang, and L. Ren, "Numerical simulation of hydrodynamic lubrication performance for continuous groove-textured surface," *Tribology International*, vol. 167, p. 107411, 2022.

[39] P. Li, F. Zhang, H. Zhang, T. Wang, Q. Wang, and W. Qiao, "Lubrication performance of kite-shaped microtexture under hydrodynamic lubrication," *Tribology International*, vol. 179, p. 108144, 2023.

[40] B. Zhu, W. Zhang, W. Zhang, and H. Li, "Generative design of texture for sliding surface based on machine learning," *Tribology International*, vol. 179, p. 108139, 2023.

[41] K. Svanberg, "MMA and GCMMA-two methods for nonlinear optimization," *vol*, vol. 1, pp. 1–15, 2007.

[42] N. Patir and H. Cheng, "An average flow model for determining effects of three-dimensional roughness on partial hydrodynamic lubrication," 1978.

[43] M. Rom, F. König, S. Müller, and G. Jacobs, "Why homogenization should be the averaging method of choice in hydrodynamic lubrication," *Applications in Engineering Science*, vol. 7, p. 100055, 2021.

[44] A. Almqvist, *On the effects of surface roughness in lubrication*. PhD thesis, Luleå Tekniska Universitet, 2006.

[45] E. Sanchez-Palencia, *Non-Homogeneous Media and Vibration Theory*. Springer-Verlag, 1980.

[46] G. Pavliotis and A. Stuart, *Multiscale methods: averaging and homogenization*. Springer Science & Business Media, 2008.

[47] S. Torquato, *Random Heterogeneous Materials: Microstructure and Macroscopic Properties*. New York, NY, USA: Springer Science & Business Media, 2002.

[48] H. G. Elrod, "Thin-film lubrication theory for newtonian fluids with surfaces possessing striated roughness or grooving," 1973.

[49] G. Bayada and M. Chambat, "Homogenization of the stokes system in a thin film flow with rapidly varying thickness," *ESAIM: Mathematical Modelling and Numerical Analysis*, vol. 23, no. 2, pp. 205–234, 1989.

[50] G. Kabacaoğlu and İ. Temizer, "Homogenization of soft interfaces in time-dependent hydrodynamic lubrication," *Computational Mechanics*, vol. 56, pp. 421–441, 2015.

[51] I. Yıldıran, İ. Temizer, and B. Çetin, "Homogenization in hydrodynamic lubrication: microscopic regimes and re-entrant textures," *Journal of Tribology*, vol. 140, no. 1, p. 011701, 2018.

[52] C. Barbarosie and A.-M. Toader, "Optimization of bodies with locally periodic microstructure," *Mechanics of advanced materials and structures*, vol. 19, no. 4, pp. 290–301, 2012.

[53] A. Keleş, İ. Temizer, and M. Cakmakci, "Homogenization-based space-time topology optimization of tunable microstructures," *International Journal for Multiscale Computational Engineering (in press)*.

[54] M. P. Bendsøe and O. Sigmund, *Topology optimization: theory, methods, and applications*. Springer Science & Business Media, 2003.

[55] O. Sigmund and J. Petersson, "Numerical instabilities in topology optimization: a survey on procedures dealing with checkerboards, mesh-dependencies and local minima," *Structural optimization*, vol. 16, pp. 68–75, 1998.

[56] A. Waseem, *Homogenization-based microscopic texture design and optimization in hydrodynamic lubrication*. PhD thesis, Bilkent Universitesi (Turkey), 2016.

[57] B. Bourdin, "Filters in topology optimization," *International journal for numerical methods in engineering*, vol. 50, no. 9, pp. 2143–2158, 2001.

[58] O. Sigmund, "Morphology-based black and white filters for topology optimization," *Structural and Multidisciplinary Optimization*, vol. 33, pp. 401–424, 2007.

[59] "Comsol multiphysics," 2018.

[60] D. J. Griffiths, "Introduction to electrodynamics," 2005.

[61] L. Dorfmann and R. W. Ogden, *Nonlinear theory of electroelastic and magnetoelastic interactions*. Springer, 2014.

Appendix A

Tensor Calculus

In this study, cartesian coordinate system is employed for the coordinates x_i with the orthonormal basis vector $\boldsymbol{e}_i$. For these parameters some of the operations are defined in this section. A vector and a 2^{nd} order tensor are

$$\boldsymbol{v} = v_i \, \boldsymbol{e}_i \quad , \tag{A.1a}$$

$$\boldsymbol{A} = A_{ij} \, \boldsymbol{e}_i \otimes \boldsymbol{e}_j \quad . \tag{A.1b}$$

Gradient operation for a scalar and a vector are

$$\nabla \phi = \frac{\partial \phi}{\partial x_j} \boldsymbol{e}_j \quad , \tag{A.2a}$$

$$\nabla \boldsymbol{v} = \frac{\partial v_i}{\partial x_j} \boldsymbol{e}_i \otimes \boldsymbol{e}_j \quad . \tag{A.2b}$$

divergence operation of a vector and a 2^{nd} order tensor are

$$\nabla \cdot \boldsymbol{v} = \frac{\partial v_i}{\partial x_i} \quad , \tag{A.3a}$$

$$\nabla \cdot \boldsymbol{A} = \frac{\partial A_{ij}}{\partial x_j} \boldsymbol{e}_i \quad . \tag{A.3b}$$

Appendix B

Finite Difference Verification of Sensitivity

The analytical sensitivities of the objective function with respect to design variables are given in comparison with the numerical sensitivities calculated via finite difference. In all examples second order derivatives are employed with the perturbation of 10^{-4}. The example in Figure 6.11 is chosen and sensitivities are calculated at the first and 150^{th} iteration of the optimization

Figure B.1 and Figure B.2 demonstrates the finite difference sensitivities of the traction-based objective function at the first and 150th step, respectively.

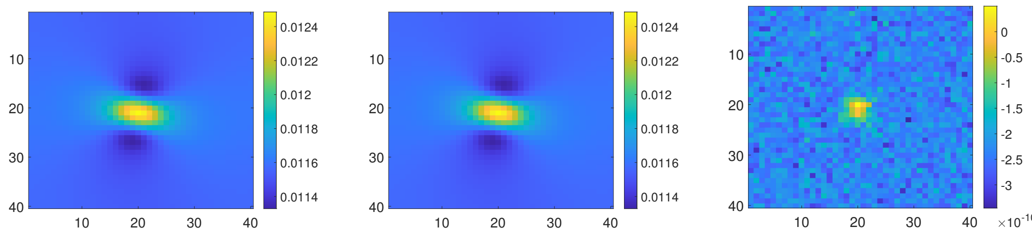

(a) Analytical sensitivity (b) Numerical sensitivity (c) Difference

Figure B.1: *Analytical and numerical sensitivities of the objective with respect to spatial design variables are provided with their differences at the beginning of optimization*

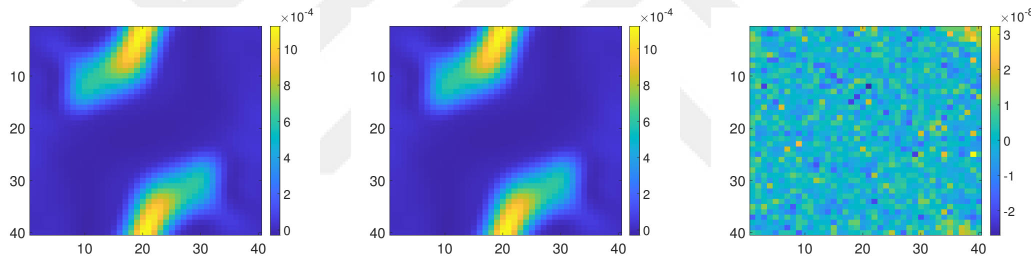

(a) Analytical sensitivity (b) Numerical sensitivity (c) Difference

Figure B.2: *Analytical and numerical sensitivities of the objective with respect to spatial design variables are provided with their differences at the* 150^{th} *iteration of optimization*

Table B.1 and B.2 demonstrates the finite difference sensitivities of the traction-based objective function with respect to temporal design variables at the first and 150th step, respectively.

t	Analytical	Numerical	Difference
1	-0.0024622340	-0.0024622215	0.1245487782e-7
2	-0.0130108413	-0.0130108347	0.0654998630e-7
3	-0.0221976803	-0.0221976767	0.0360138480e-7
4	-0.0292554008	-0.0292554007	0.0013485087e-7
5	-0.0335752974	-0.0335753001	-0.0270258165e-7
6	-0.0345662093	-0.0345662161	-0.0679310395e-7
7	-0.0337347108	-0.0337347203	-0.0943006001e-7
8	-0.0338742577	-0.0338742669	-0.0918487643e-7
9	-0.0343382931	-0.0343382992	-0.0608917442e-7
10	-0.0326463890	-0.0326463906	-0.0153126369e-7
11	-0.0315997258	-0.0315997259	-0.0010872714e-7
12	-0.0333571061	-0.0333571085	-0.0235517336e-7
13	-0.0344352585	-0.0344352621	-0.0357651495e-7
14	-0.0306661054	-0.0306661067	-0.0128295857e-7
15	-0.0212226485	-0.0212226447	0.0382907472e-7
16	-0.0100013720	-0.0100013637	0.0834960393e-7
17	-0.0006508876	-0.0006508744	0.1315858227e-7
18	0.0031609454	0.0031609623	0.1690580762e-7

Table B.1: Analytical and numerical sensitivities of the objective with respect to temporal design variables are provided with their differences at the beginning of optimization

t	Analytical	Numerical	Difference
1	0.0000591548	0.0000591768	0.0021960229e-5
2	0.0005480756	0.0005481085	0.0032949151e-5
3	0.0006748594	0.0006749171	0.0057627730e-5
4	0.0012779458	0.0012781041	0.0158252530e-5
5	0.0019203534	0.0019208895	0.0536045398e-5
6	-0.0131105541	-0.0131094056	0.1148543659e-5
7	-0.0378626524	-0.0378619298	0.0722631177e-5
8	-0.0369565005	-0.0369557094	0.0791097835e-5
9	-0.0126309844	-0.0126300649	0.0919486528e-5
10	0.0016001526	0.0016004784	0.0325831684e-5
11	0.0013986429	0.0013988015	0.0158536366e-5
12	0.0013616982	0.0013620538	0.0355611162e-5
13	0.0026675945	0.0026681739	0.0579472640e-5
14	0.0018143553	0.0018146489	0.0293569442e-5
15	0.0008148808	0.0008149533	0.0072517298e-5
16	0.0004360398	0.0004360712	0.0031379504e-5
17	0.0000697626	0.0000697840	0.0021425571e-5
18	0.0001403991	0.0001404145	0.0015483220e-5

Table B.2: Analytical and numerical sensitivities of the objective with respect to temporal design variables are provided with their differences at the 150^{th} iteration of optimization

Table B.3 and B.4 demonstrates the finite difference sensitivities of the traction-based objective function with respect to geometry design variables at the first and 150th step, respectively.

P_{ij}	Analytical	Numerical	Difference
P_{11}	0.282638 e-5	0.282640 e-5	1.398167 e-11
P_{12}	-2.009766 e-5	-2.009771 e-5	-4.343220 e-11
P_{21}	-2.009766 e-5	-2.009771 e-5	-4.281294 e-11
P_{22}	-0.282631 e-5	-0.282640 e-4	-8.852581 e-11

Table B.3: Analytical and numerical sensitivities of the objective with respect to geometry design variables are provided with their differences at the first iteration of optimization

P_{ij}	Analytical	Numerical	Difference
P_{11}	-0.0002631	-0.0002632	-0.0417608e-06
P_{12}	-0.0002691	-0.0002691	-0.0069220 e-06
P_{21}	0.0032425	0.0032428	0.3585459 e-06
P_{22}	-0.0001681	-0.0001682	-0.0064568 e-06

Table B.4: Analytical and numerical sensitivities of the objective with respect to geometry design variables are provided with their differences at the 150^{th} iteration of optimization

It is noted that 0.01 % difference is the practical limit for a second order sensitivity analysis, better match can be obtained by a higher order difference scheme. However, increasing the order would require more data points; which would be computationally more expensive. Therefore 0.01 % difference is chosen which is satisfactory for the verification purposes.

Appendix C

Electrostatics Problem Verifications

In this section, the proposed double-electrode design by Visshers et al [?] is tested for the electrostatic simplifications applied in the analysis in Chapter 7. First, the model is created by following the exact sizes of the elastomer and electrodes, as provided within that study. Additionally, air and substrate environments are added. The corresponding analysis is provided in Figure C.1.

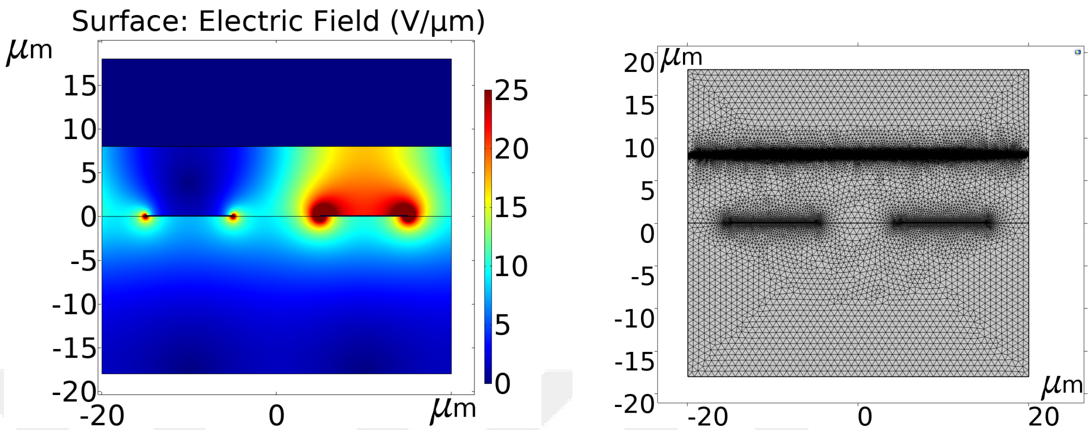

(a) Electric field (b) Mesh

Figure C.1: *Crossection of the proposed double electrode unit cell is modeled with thin electrode domains considering air on top of the material and a glass substrate, similar to proposed structure by [1]. On the left, developed electric field is demonstrated for the given mesh on the right*

Subsequently, the environments are eliminated from the system and it is verified that there is no significant change on the generated electric field in Figure C.2.

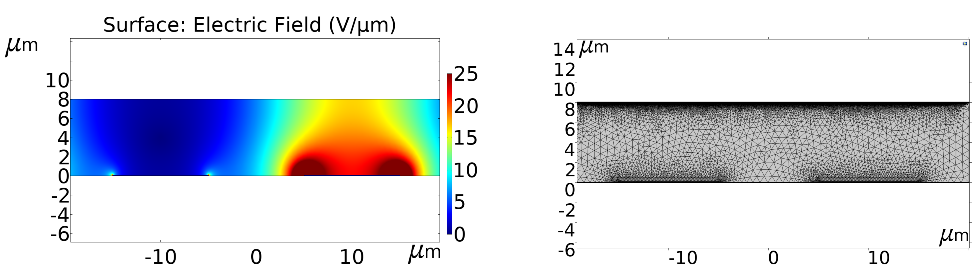

(a) Electric field (b) Mesh

Figure C.2: *Crossection of the proposed double electrode unit cell is modeled with thin electrode domains without considering environment. On the left, developed electric field is demonstrated for the given mesh on the right*

Finally, thin electrodes are also eliminated from the system and voltages are instead assigned on the surface of material with a uniform mesh in Figure C.3.

This form significantly reduces the degrees of freedom and delivered very close results to the fully realized case in Figure C.1.

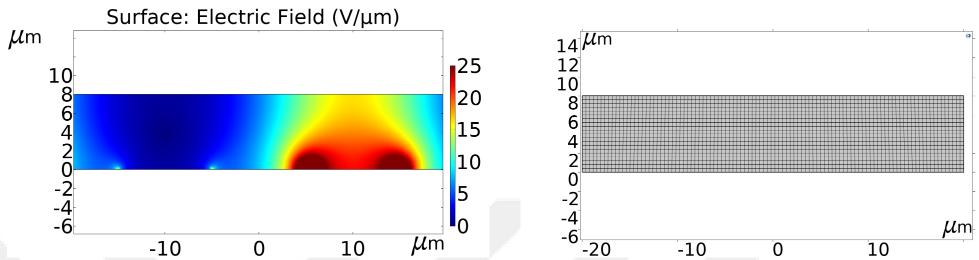

(a) Electric field

(b) Mesh

Figure C.3: *Crossection of the proposed double electrode unit cell is modeled with employing only the elastomer and assigning electrodes as surface voltages. On the left, developed electric field is demonstrated for the given mesh on the right*

After these assumptions, it is observed that the electric field in the vicinity of the deformable surface remains nearly unmodified. Because the tractions are solely determined by the electric field in this region it can be concluded that these numerically efficient simplifications are reasonable.

Appendix D

Three Dimensional Discretization

It is observed that mesh selection dramatically affects the results of the problems. In coarse resolutions, free tetrahedral meshes may display irregular surface deformations (Figure D.1). On the other hand, uniform quadrilateral meshes are observed to be free of such local disturbances (Figure D.2).

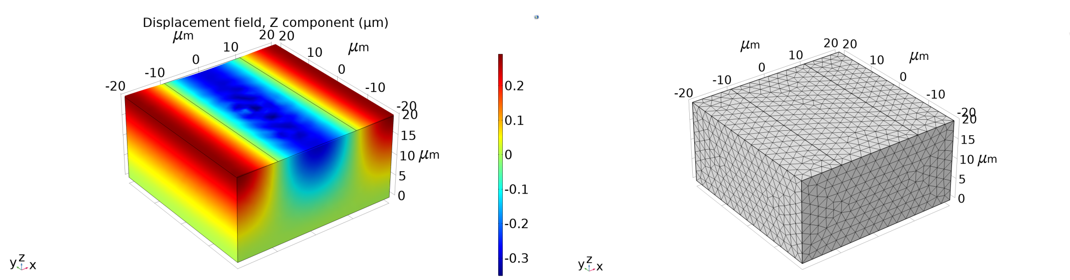

(a) Electric field (b) Mesh

Figure D.1: *Coupled modeled built with free tetrahedral meshes which can be solved up to 550V.*

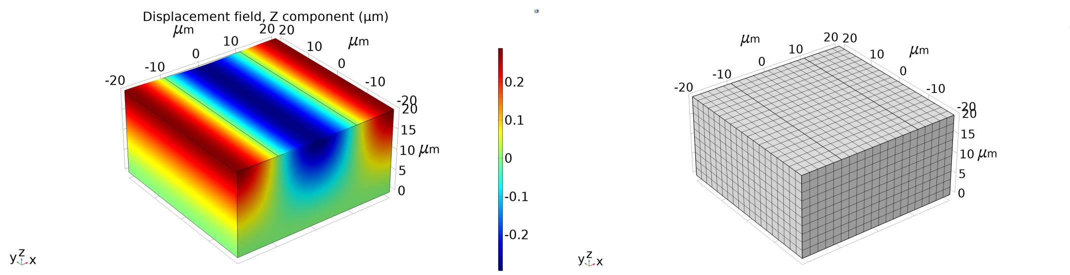

(a) Electric field

(b) Mesh

Figure D.2: *Coupled modeled built with free tetrahedral meshes which can be solved up to 1000V. Here 550V is applied for the comparaison between images.*

Appendix E

Full Range Texture Motion and Preconditioning

The variable τ is chosen to be between 0 and 1 in the present setting, meaning that the active surface can move between a completely smooth surface and a textured structure. However, it is possible to invert the structure by allowing a full range of motion as shown in the Figure E.1 by expanding the interval for τ between [-1,1]. While giving minimum and maximum values for design variables to MMA, bounds are set as 0 for the minimum and 1 for the maximum for all design variables. Therefore, in order to use τ between [-1,1] , one can map the design variable k to $k' = 2(k - 0.5)$ and use k' to obtain filtered variable τ. Allowing texture inversion provides a wider range for texture tunability. On the other hand, it also makes the system more vulnerable to non-uniqueness.

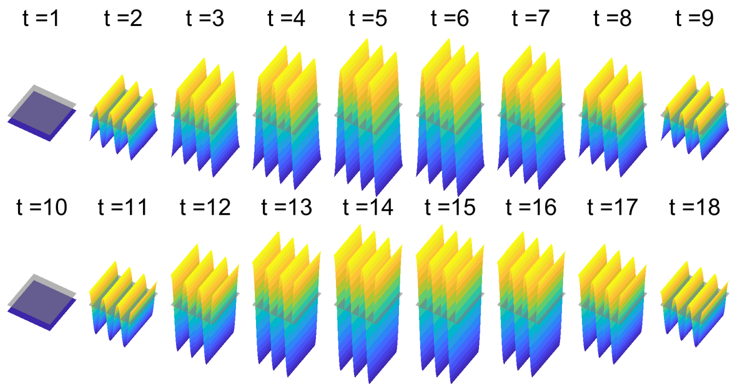

Figure E.1: *Active surface motion for one time period with inversion*

In some cases, non-uniqueness is not a major problem, for instance in the time optimization depicted in Figure E.2. Here, the inverted texture is exactly the same as the original one due to non-uniqueness of the setting and periodicity. In such a setting, an inversion corresponds to the same overall response. As a result, the design variable picks a variation that differs from the target input as depicted in figure E.2(b). Note that the filter disturbs the transition points, but this is not a problem because the targeted flux response is already captured sufficiently well.

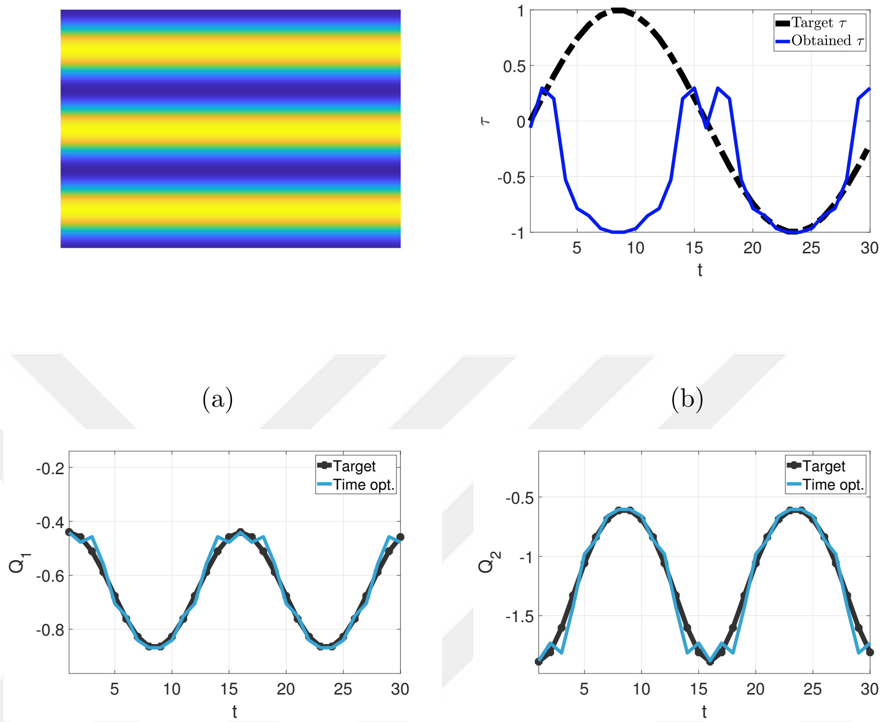

(a) (b)

(c) (d)

Figure E.2: *A suboptimal result due to (-1,1) interval chosen for τ is demonstrated. Texture has $\bar{h}^+ = 2.5$, $\bar{h}^- = 0.8$ and $h_0 = 1.65$ due to symmetric distribution of peaks and valleys.*

On the other hand, if the surface texture is not symmetric with respect to the peaks and valleys (Figure E.3) then optimization can get stuck at a local minima. It is observed that the average film thickness constraint is satisfied but the targeted response cannot be captured by the emerging result. This scenario can be prevented by applying a preconditioning to the system.

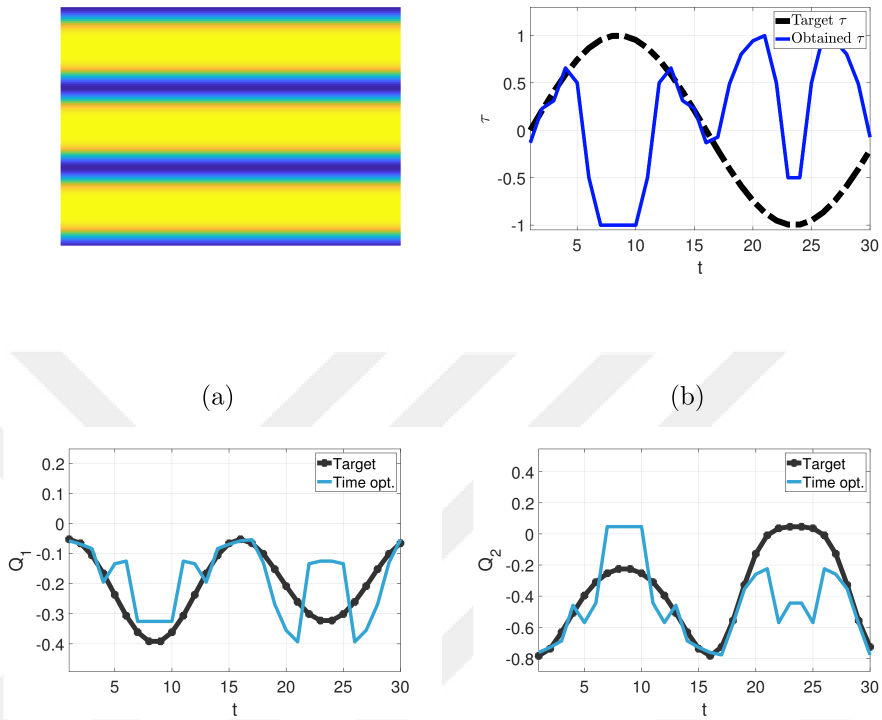

(a) (b)

(c) (d)

Figure E.3: *A suboptimal result due to (-1,1) interval chosen for τ is demonstrated for a non-symmetric texture which has $\bar{h}^{+} = 2.5$, $\bar{h}^{-} = 0.8$ and $h_0 = 1.31$.*

Within preconditioning, at every n^{th} time steps, a scanning for a better τ value is carried out until the solution is satisfactory. For each time step 10 potential values are uniformly chosen from the interval (-1,1) for τ and by using each one a new objective value is evaluated. This objective is compared with the current value of the objective and replaced if it is better. The version of Figure E.3 which is improved via this scheme is demonstrated in Figure E.4.

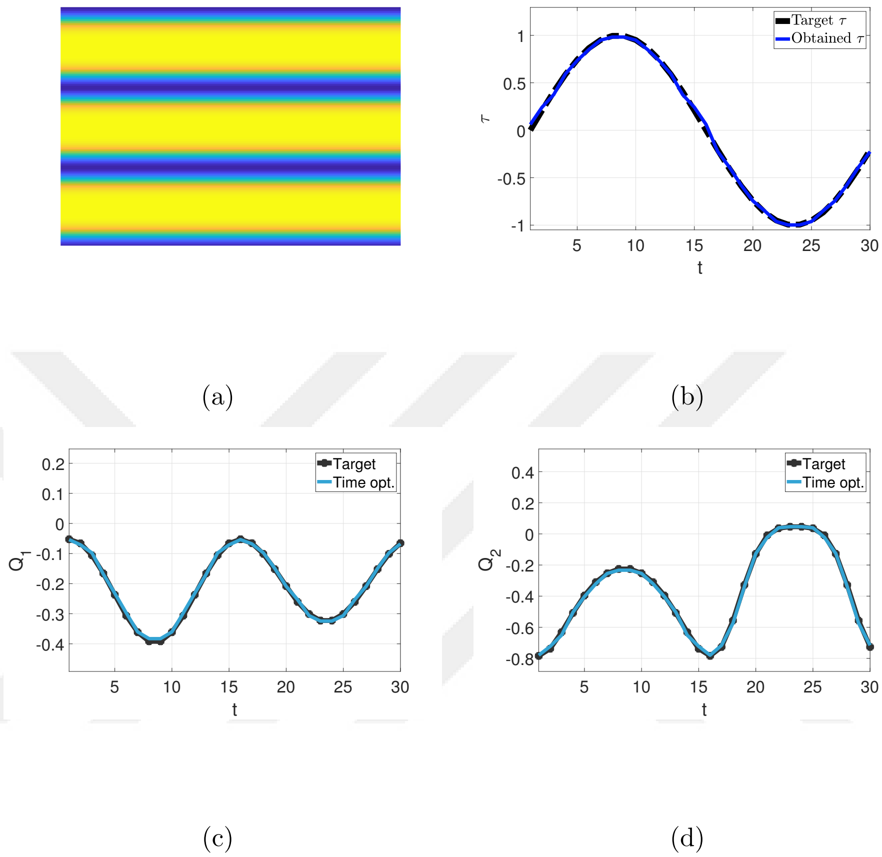

Figure E.4: *Result of macroscopic flux optimization with preconditioning which is applied to fix the suboptimal result due to (-1,1) interval chosen for* τ*. Texture is non-symmetric with the values* $\bar{h}^+ = 2.5$*,* $\bar{h}^- = 0.8$ *and* $h_0 = 1.31$.

Despite its effectiveness on solving problems that are stuck on local minima, preconditioning has a limited capacity to enhance the framework. When it is employed with the filter, its effectiveness decreases because individual time steps lose their independence and the best τ value for each time step does not necessarily correspond the best $\boldsymbol{\tau}$ for the system. Also, when other optimization schemes are introduced other than time, preconditioning loses its effectiveness because other sources of non-uniqueness emanate in the system.

Appendix F

Projection for Double electrode Unit Cells

In addition to preconditioning, there are other aspects to be considered for a full range of texture motion such as projection for the 3D realization. For an inverted surface there has to be two sets of electrodes at the bottom of the elastomer with exchanging voltages as it was in the previously demonstrated case of double electrodes in Figure 7.1(a). For such a case, projection does not have to divide domain to two strict subdomains, but instead it should create a transition area to seperate electrodes from each other as shown in Figure F.1.

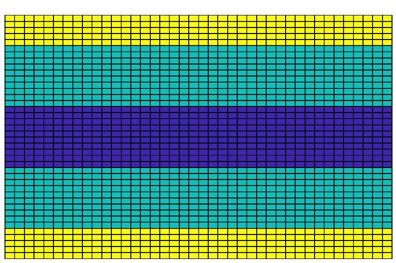

(a) 25% Amplitude projection

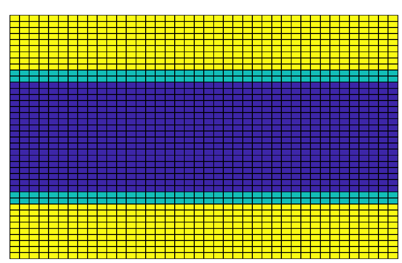

(b) 75% Amplitude projection

Figure F.1: *Projections of the microtextures are illustrated where different percentages of the amplitude of the deviation is projected as the area which electrodes should cover.*